

**THEORETICAL LIMITS AND SAFETY CONSIDERATIONS FOR
MAGNETO-ACOUSTO ELECTRICAL TOMOGRAPHY**

A THESIS SUBMITTED TO
THE GRADUATE SCHOOL OF NATURAL AND APPLIED SCIENCES
OF
MIDDLE EAST TECHNICAL UNIVERSITY

BY
ELYAR GHALICHI

IN PARTIAL FULFILLMENT OF THE REQUIREMENTS
FOR
THE DEGREE OF MASTER OF SCIENCE
IN
ELECTRICAL AND ELECTRONICS ENGINEERING

FEBRUARY 2017

Approval of the thesis:

**THEORETICAL LIMITS AND SAFETY CONSIDERATIONS FOR
MAGNETO-ACOUSTO ELECTRICAL TOMOGRAPHY**

submitted by **ELYAR GHALICHI** in partial fulfillment of the requirements for the degree of **Master of Science in Electrical and Electronics Engineering Department, Middle East Technical University** by,

Prof. Dr. Gülbin Dural Ünver
Dean, Graduate School of **Natural and Applied Sciences** _____

Prof. Dr. Tolga Çiloğlu
Head of Department, **Electrical and Electronics Engineering** _____

Prof. Dr. Nevzat Güneri Gençer
Supervisor, **Electrical and Electronics Engineering Department, METU** _____

Examining Committee Members:

Prof. Dr. Murat Eyüboğlu
Electrical and Electronics Engineering Department, METU _____

Prof. Dr. Nevzat Güneri Gençer
Electrical and Electronics Engineering Department, METU _____

Prof. Dr. Mustafa Kuzuoğlu
Electrical and Electronics Engineering Department, METU _____

Assoc. Prof. Dr. Yeşim Serinağaoğlu Doğrusöz
Electrical and Electronics Engineering Department, METU _____

Assist. Prof. Dr. Özlem Birgül
Biomedical Engineering Department, Ankara University _____

Date: 17.02.2017

I hereby declare that all information in this document has been obtained and presented in accordance with academic rules and ethical conduct. I also declare that, as required by these rules and conduct, I have fully cited and referenced all material and results that are not original to this work.

Name, Last Name: ELYAR GHALICHI

Signature :

ABSTRACT

THEORETICAL LIMITS AND SAFETY CONSIDERATIONS FOR MAGNETO-ACOUSTO ELECTRICAL TOMOGRAPHY

Ghalichi, Elyar

M.S., Department of Electrical and Electronics Engineering

Supervisor : Prof. Dr. Nevzat Güneri Gençer

February 2017, 60 pages

In this study, the performance of Magneto-Acousto-Electrical Tomography (MAET) method is investigated quantitatively by considering interrelations between its sensitivity, resolution and conductivity contrast. An analytical solution for the forward problem of MAET is derived for two-dimensional (2D) concentric bodies by Separation of Variables Method. The electric potential and the acoustic pressure are separated to their angular and radial components. The series coefficients for these solutions are obtained by their respective boundary conditions. These analytical solutions are compared to the numerical solutions calculated by COMSOL Multiphysics. The relative errors between these two solutions for electric potential and acoustic pressure are obtained. In both cases, the average relative error is below one percent. The electric potential on the boundary is related to the acoustic boundary acceleration analytically. From this potential expression, a sensitivity expression is derived relating fractional change in conductivity contrast to fractional change in the measured electric potential. This expression is a function of resolution and conductivity contrast of the imaging system. It also depends on the acoustic wave number and the dimensions of the body. The pair-wise relation between these parameters are presented. The sensitivity behavior of MAET is compared with Electrical Impedance Tomography and the improvements for small inhomogeneities are presented. For eccentric bodies, a modified expression for the sensitivity is obtained by conformal mapping. For arbi-

trary periodic boundary excitations, the sensitivity expressions of harmonic cases are combined to obtain a unified sensitivity expression.

Moreover, the tissue heating concerns arising in MAET imaging method is investigated numerically for a simplified 2D breast model. The steady state temperature distribution in the model is evaluated for an external source free case. The medium is excited with a 16 element linear phased array transducer at 1 MHz. The amplitude of acoustic excitation is set to the mechanical safety limit (1.7 MPa) at 1 MHz. The heating profiles due to acoustic absorption and resistive Lorentz current dissipation are demonstrated. The maximum temperature change is below 1 Kelvin and within the thermal safety limits.

Keywords: Separation of variables method, COMSOL Multiphysics, Magneto-Acousto Electrical Tomography, Analytical solution, Sensitivity analysis

ÖZ

MANYETO AKUSTO ELEKTRİKSEL TOMOGRAFİNİN TEORİK SINIRLARI VE GÜVENLİK ÇALIŞMALARI

Ghalichi, Elyar

Yüksek Lisans, Elektrik ve Elektronik Mühendisliği Bölümü

Tez Yöneticisi : Prof. Dr. Nevzat Güneri Gençer

Şubat 2017 , 60 sayfa

Bu çalışmada, Magneto-Akusto-Elektriksel Tomografi (MAET) metodunun performansı, duyarlılığı, çözünürlüğü ve iletkenlik kontrastı arasındaki ilişkiler kantitatif (nicel) olarak incelenmiştir. Bu işlemi yapmak için, MAET'in ileri probleminde bileşkelere ayırma metodunu uygulanarak iki boyutlu (2B) eş merkezli cisimler için analitik bir ifade elde edilmiştir. Elektriksel potansiyel ve akustik basınç, açılma ve radyal bileşenlerine ayrılmıştır. Sınır koşulları kullanılarak seri açılım katsayıları bulunmaktadır. Bu analitik çözümler COMSOL çoklu fizik yazılımıyla elde edilen sayısal çözümler ile kıyaslanmaktadır. Bu çözümler arasındaki nispi hatalar sunulmaktadır. Sonlu elemanlar metodundaki bütün ağ noktaları için bu hatalar hesaplanmıştır. Her iki durumun da, elektrik potansiyel ve akustik basınç, nispi hataları yüzde birin altındadır. Sınırdaki ölçülen elektrik potansiyeli analitik olarak uygulanan akustik sınır ivme ile ilişkilendirilmiştir. Bu potansiyel ifadesinden, elektriksel potansiyeldeki oransal değişim ile iletkenlik kontrastındaki oransal değişimi ilişkilendiren bir duyarlılık ifadesi elde edilmiştir. Bu ifade görüntüleme sisteminin çözünürlüğü, iletkenlik kontrastına, akustik dalga sayısı ve cismin boyutlarına bağlıdır. Bu parametrelerin arasındaki ikili ilişkiler gösterilmiştir. MAET'in duyarlılık karakteristiği Elektriksel Empedans Tomografi ile karşılaştırılmıştır ve küçük çözünürlük değerlerindeki gelişmeler gösterilmiştir. Eş merkezli olmayan cisimler için, açı korur gönderim yöntemi ile bir duyarlılık ifadesi elde edilmiştir. Harmonik olmayan akustik uyarımlar için,

harmonik uyarımların duyarlılık ifadesinin birleştirilmesi ile genel bir duyarlılık ifadesi elde edilmiştir.

Ayrıca, 2B basit bir göğüs modeli için MAET görüntüleme yöntemindeki ısınma problemi sayısal olarak incelenmiştir. Harici kaynağın olmadığı durumda vücut içerisindeki sabit ısı dağılımı hesaplanmıştır. Daha sonra cisim 1 saniye boyunca 16 elemanlı akustik dönüştürücü ile uyarılmıştır. Akustik emilimden ve dirençsel Lorentz akımlarından kaynaklanan güç yitiminden (kaybından) kaynaklanan ısı profili gösterilmiştir. Azami ısı artışı 1 Kelvin'in altındadır ve güvenlik limitleri içerisinde.

Anahtar Kelimeler: değişkenlerine ayırma yöntemi, COMSOL Çoklufizik, Manyeto Akusto Elektriksel Tomografi, Analitik çözüm, Duyarlılık analizi

To my family

ACKNOWLEDGMENTS

I would like to express my sincere gratitude to my supervisor Professor Nevzat Güneri Gençer for the support of my research, for his motivation, guidance and enthusiasm. May it be in my graduate studies or life in general, the skill and experience i gained throughout my master's degree under supervision of Professor Gençer will be of utmost importance.

I would like to thank Professor Mustafa Kuzuoğlu for his time and guidance at the early stage of my thesis work. I also would like to thank Dr. Reyhan Zengin for her support, friendship and contribution to my research. It was a quite rewarding learning experience to work in the same research group. I am thankful to Associate Professor Theodoros Samaras for evaluation of my work during a conference and offering a suggestion that has found its way in my thesis.

Throughout my master's studies, the companion of friends at bioelectromagnetic research lab has been invaluable to me. Dr. Azadeh Kamali Tafreshi has been quite welcoming and supportive since the day i joined the research group. I am thankful for her kindness and guidance. I would like to thank Mehmet Soner Gözü for his friendship, motivation and helpfulness in stressful times. I also would like to thank my dear friends Keivan Kaboutari and Ahmet Önder Tetik for their support all along.

Lastly, sincerest thanks to my family members who have always been by my side and supported me through difficult times.

This research was generously supported by Scientific and Technical Research Council of Turkey (TÜBİTAK) under the 114E184 (COST Action BM1309).

TABLE OF CONTENTS

ABSTRACT	v
ÖZ	vii
ACKNOWLEDGMENTS	x
TABLE OF CONTENTS	xi
LIST OF TABLES	xiii
LIST OF FIGURES	xiv
LIST OF SYMBOLS AND ABBREVIATIONS	xvii
CHAPTERS	
1 INTRODUCTION	1
2 ANALYTICAL SOLUTION OF MAET	5
2.1 Acoustic Problem	5
2.2 Electrical Problem	8
3 ACCURACY OF THE ANALYTIC SOLUTIONS	11
3.1 Acoustic Problem	11
3.2 Electrical Problem	14
4 SENSITIVITY ANALYSIS FOR MAET	23

4.1	Deriving the Sensitivity Expression	23
4.2	Pair-wise Relations	27
4.2.1	Sensitivity-Resolution	27
4.2.2	Sensitivity-Conductivity Contrast	31
4.2.3	Sensitivity-Outer Radius	31
4.2.4	Sensitivity-Acoustic Attenuation	33
4.2.5	Sensitivity-Frequency	33
4.2.6	Resolution-Conductivity Contrast	36
4.2.7	Summary of Pair-wise Relations	36
4.3	Conformal Mapping (Eccentric Inhomogeneities)	36
4.4	Comparison to EIT Sensitivity	38
4.5	Arbitrary Periodic Boundary Excitations	38
5	HEAT ANALYSIS FOR MAET	43
5.1	Acoustic Problem	43
5.2	Electrical Problem	45
5.3	Heat Problem	47
6	CONCLUSION	53
6.1	Summary	53
6.2	Discussion	53
6.3	Future Work	55
	REFERENCES	57

LIST OF TABLES

TABLES

Table 4.1	Dispersion parameters for fat and blood tissue [24].	34
Table 5.1	The acoustic properties of breast tissue at 1 MHz [27].	44
Table 5.2	The electrical properties of breast tissues at 1 MHz [30–32].	46
Table 5.3	Breast tissues and tumor’s thermal properties [35].	48

LIST OF FIGURES

FIGURES

<p>Figure 1.1 2D concentric circle geometry of MAET in x-y coordinates. Here \mathbf{B}_0 is static magnetic field density normal to the plane (z-direction) and ϕ is the electric potential distribution. Inner circle's radius and electrical conductivity are represented by R_1 and σ_1. The outer circle's radius is R_2 and its conductivity is denoted by σ_2.</p>	2
<p>Figure 3.1 (a) The analytical and (b) numerical acoustic pressure distributions inside a homogeneous circle of radius $R_2 = 5$ cm. First harmonic boundary acceleration is applied and acoustic properties of the gland tissue are assumed. The acoustic pressure distribution close to the origin is magnified to enhance its details.</p>	13
<p>Figure 3.2 Location of points with relative error (acoustic pressure's magnitude) greater than 10 % (32 points) and a phase difference greater than 5° (29 points).</p>	14
<p>Figure 3.3 Concentric circle geometry with an acoustic point source Q.</p>	15
<p>Figure 3.4 (a) The analytical and (b) numerical magnitude of electric potential in 2D concentric circles. The potential is maximum close to acoustic source. The radius of the concentric inhomogeneity is 6.25 mm.</p>	17
<p>Figure 3.5 Location of points with relative error (electric potential's magnitude) greater than 5 % and phase difference of greater than 2°. The other points of FEM mesh have lower errors in absolute value and phase.</p>	18
<p>Figure 3.6 The average relative error in absolute value of electric potential between the analytical and numerical solutions as a function of number of terms in series expansion ($R_1 = 6.25$ mm).</p>	19
<p>Figure 3.7 (a) The analytical and (b) numerical magnitude of electric potential in 2D concentric circles. The potential is maximum close to acoustic source. The radius of the concentric inhomogeneity is 3.125 mm.</p>	20

Figure 3.8	Location of points with relative error (electric potential's magnitude) greater than 5 % and phase difference of greater than 2° . The other points of FEM mesh have lower errors in absolute value and phase.	21
Figure 3.9	The average relative error in absolute value of electric potential between the analytical and numerical solutions as a function of number of terms in series expansion ($R_1 = 3.125$ mm).	21
Figure 4.1	The sensitivity of MAET as a function of m for different resolution values in (a) and different conductivity contrast values in (b).	26
Figure 4.2	(a) The distribution of the absolute value of acoustic pressure and (b) the absolute value for θ component of acoustic velocity along the x axis. These distributions are radially symmetric.	28
Figure 4.3	Sensitivity and divergence of Lorentz current as a function of resolution. (a) Real components, (b) Imaginary components ($\alpha = 1$, $a = 8.635$ Np/m and $R_2 = 5$ cm).	29
Figure 4.4	The sensitivity versus resolution plot for different conductivity contrast values. For sufficiently small resolution (β) values, sensitivity is higher when conductivity contrast approaches unity ($a = 8.635$ Np/m and $R_2 = 5$ cm).	30
Figure 4.5	The logarithmic sensitivity versus conductivity contrast plot for different resolution values ($a = 8.635$ Np/m and $R_2 = 5$ cm).	32
Figure 4.6	The logarithmic, sensitivity versus outer radius plot is given for different resolution values ($\alpha = 1$, $a = 8.635$ Np/m and $R_2 = 5$ cm).	32
Figure 4.7	The logarithmic sensitivity versus acoustic attenuation plot for different resolution values ($\alpha = 1$ and $R_2 = 5$ cm).	33
Figure 4.8	The logarithmic sensitivity versus frequency plot for different resolution values ($\alpha = 1$ and $R_2 = 5$ cm).	35
Figure 4.9	The logarithmic, resolution versus conductivity contrast plot for different sensitivity values.	35
Figure 4.10	Conformal mapping from z -domain to w -domain, defined by function $w(z)$ in (4.19).	37
Figure 4.11	The sensitivity of MAET and EIT as a function of resolution for (a) $m = 1$ and (b) $m = 2$. The conductivity contrast is unity in both cases.	39
Figure 4.12	The square pulse centered at $\theta = \pi/2$ and angular length of $\pi/3$	40

Figure 4.13 The sensitivity distribution of harmonic and non-harmonic excitations at $\theta = 0$ and $\theta = \pi/3$	41
Figure 5.1 A simplified 2D breast model composed of subcutaneous fat, gland, tumor, muscle and thoracic muscle tissues [26].	44
Figure 5.2 The modified breast model with the introduction of 16 element LPA transducer. The LPA elements (blue lines) are modeled as normal boundary acceleration.	45
Figure 5.3 The steady state magnitude of acoustic pressure intensity in the simplified 2D breast model.	46
Figure 5.4 The total current density distribution in the simplified 2D breast model.	47
Figure 5.5 The steady state heat distribution in absence of electrical and acoustic heat sources.	48
Figure 5.6 (a) The distribution of acoustic heat source and (b) electric heat source in the simplified 2D breast model.	50
Figure 5.7 The heat distribution at (a) $t = 1$ s and (b) $t = 10$ s, where the tissue is acoustically excited for a second.	51
Figure 5.8 The temperature increase in the simplified 2D breast model at $t = 1$ s relative to its initial value.	52

LIST OF SYMBOLS AND ABBREVIATIONS

SYMBOLS

Ω	Bounded Domain	
$d\Omega$	Boundary	
x	x Coordinate	m
y	y Coordinate	m
z	z Coordinate	m
r	Radial Coordinate	m
θ	Angular Coordinate	rad
\mathbf{a}_r	Radial Unit Vector	
\mathbf{a}_θ	Angular Unit Vector	
\mathbf{a}_z	z Coordinate Unit Vector	
ϕ	Electric Potential	V
ϕ_1	Electric Potential in Inner Circle	V
ϕ_2	Electric Potential in Outer Ring	V
\mathbf{B}_0	Static Magnetic Flux Density	T
σ	Electrical Conductivity	S/m
σ_1	Electrical Conductivity of Inner Circle	S/m
σ_2	Electrical Conductivity of Outer Ring	S/m
R_1	Radius of the Inner Circle	m
R_2	Outer Radius of the Ring	m
p	Acoustic Pressure	Pa
k	Acoustic Wave Number	1/m
\mathbf{n}	Unit Normal Vector	
ρ	Density	kg/m ³
c	Sound Speed	m/s
a	Acoustic Attenuation	Np/m
f	Frequency	Hz
a_n	Acoustic Boundary Acceleration	m/s ²

$R(r)$	Radial Component of SVM	
$\Theta(\theta)$	Angular Component of SVM	
m	Index of SVM Summation	
A_m, B_m	Series Coefficient of Acoustic Pressure	Pa
$\mathbf{J}_{Lorentz}$	Lorentz Current Density	A/m ²
\mathbf{v}	Acoustic velocity	m/s
e_m, f_m	Series Coefficients of Electric Potential	V
a_m, b_m, c_m, d_m	Series Coefficients of Electric Potential	V
Q	Acoustic Flow rate	m ² /s
$\mathbf{r} : (r, \theta)$	Field Point	m
$\mathbf{r}_s : (r_s, \theta_s)$	Source Point	m
R	Distance From Source Point to Field Point	m
ω	Angular Frequency	rad/s
γ_m, δ_m	Fourier Coefficients of Acoustic Boundary Acceleration	m/s ²
ζ_m^1, η_m^1	Fourier Series Coefficients of Divergence of Lorentz current on R_1	A/m ³
ζ_m^2, η_m^2	Fourier Series Coefficients of Divergence of Lorentz current on R_2	A/m ³
z_{mm}	Driving Point Impedance	Vs ² /m
S_m	Sensitivity	
α	Conductivity Contrast	
β	Resolution	
η	Material Parameter for Attenuation	
ε'	Relative Complex Permittivity	
ε_∞	Permittivity at $\omega T \gg 1$	
$\Delta\varepsilon_n$	Magnitude of Dispersion	
τ_n	Polarization Constant	s
α_n	Distribution Parameter	
σ_{DC}	DC Electrical Conductivity	S/m
Z_i	Acoustic Impedance of Air	kg/(m ² ·s)
ω_e	Electric Angular Frequency	rad/s
T	Temperature	°C
C_p	Specific Heat Capacity	J/(kg·K)
k_T	Thermal Conductivity W/(m·K)	

Q	Heat Sources	W/m^3
ω_b	Blood Perfusion Rate	$1/s$
ϵ	Emissivity	
σ_{S-B}	Stefan-Boltzmann Constant	$W/(m^2 \cdot K^4)$
h	Total Heat Transfer Coefficient	$W/(m^2 \cdot K)$
I	Acoustic Intensity	W/m^2
J	Electric Current Density	A/m^2

ABBREVIATIONS

EIT	Electrical Impedance Tomography
MAET	Magneto-Acousto Electrical Tomography
LFEIT	Lorentz Field Electrical Impedance Tomography
2D	Two-Dimensional
SVM	Separation of variables method
LPA	Linear Phased Array
BDF	Backward Differentiation Formula

CHAPTER 1

INTRODUCTION

Electrical impedance tomography (EIT) is a noninvasive technique to image the conductivity distribution of an object [1–5]. EIT system's spatial resolution is limited by number of electrodes in regions close to surface. Seagar et. al. [6] showed quantitatively that EIT's spatial resolution is limited by number of electrodes in regions close to surface. Also, the current density inside the object is lower than the current density on the surface hence the spatial resolution is poorer in these regions. Hybrid imaging methods are proposed to improve the spatial resolution of EIT. One such method, Magneto-Acousto-Electrical Tomography (MAET), combines ultrasound with electrical impedance tomography [7–15]. In the existence of a static magnetic field, the resultant (velocity) current density is sensed by a receiver coil encircling the body or electrodes attached to the body (Fig. 1.1). The main objective of this study is to obtain an analytic solution for the forward problem of MAET and investigate its theoretical limits, i.e., its sensitivity, resolution and conductivity contrast.

Analytical solutions are essential in investigating the performance of an imaging system quantitatively. Analytical solutions of EIT are investigated in [5, 16–19]. Separation of variables method (SVM) is the most common method to solve the forward problem of EIT. SVM is applicable to geometries with constant coordinate boundaries. One popular geometry for SVM, which is the concern of this study also, is two dimensional (2D) concentric circles in polar coordinates [5, 16]. In addition, different 2D geometries are studied in rectangular and elliptic coordinates [16]. 3D studies are established in [17] for variety of coordinate systems and conductivity distributions. For eccentric circles conformal mapping is utilized in 2D polar coordinates [5, 18, 19].

In [19] both conductivity and permittivity are considered in obtaining electric potential.

In a recent thesis study SVM is applied to reciprocal problem of Lorentz Field Electrical Impedance Tomography (LFEIT) in homogeneous medium [9]. Although this approach does not provide the potential and magnetic field distributions in the domain that could be measured experimentally, it's possible to calculate the voltage induced in the coil with numerical integration of obtained electric field distribution in reciprocal problem over the entire domain.

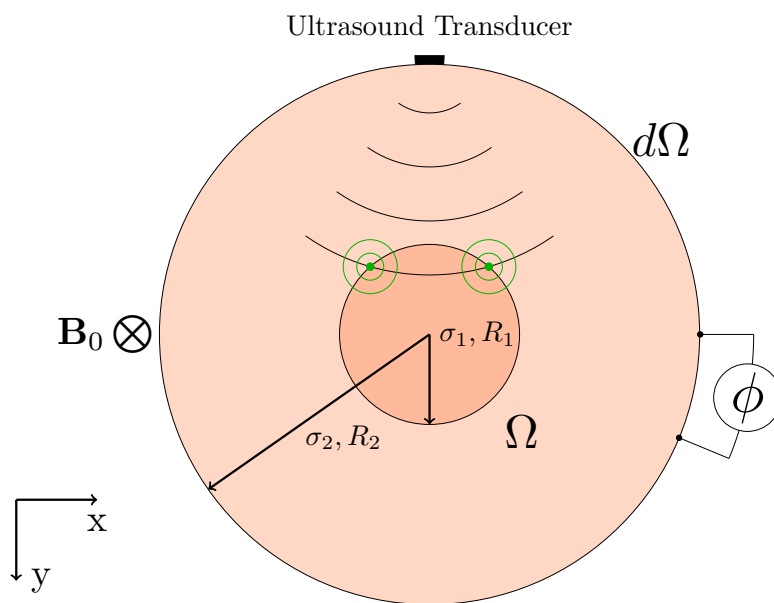


Figure 1.1: 2D concentric circle geometry of MAET in x-y coordinates. Here B_0 is static magnetic field density normal to the plane (z-direction) and ϕ is the electric potential distribution. Inner circle's radius and electrical conductivity are represented by R_1 and σ_1 . The outer circle's radius is R_2 and its conductivity is denoted by σ_2 .

In this study, an analytical solution is obtained for forward problem of MAET in 2D polar coordinates. Unlike EIT, in MAET the electric potential distribution is complex valued function, since for acoustic excitation of 1 MHz the acoustic wavelength is much smaller than the length of the body of interest. The forward problem in 2D polar coordinates is separated to angular and radial components. In order to span the space of complex functions, the solution for angular distribution is obtained by

complex exponential harmonics. This forward problem is also solved numerically by COMSOL Multiphysics [17] based on Finite Element Method (FEM). The analytic solution of electric potential is calculated on each node of FEM mesh. The electric potential plots for both solutions are presented. The relative error for phase and magnitude of these solutions is also calculated.

In chapter 2, analytical solutions for acoustic and electrical problems of MAET are derived based on SVM. The coefficients of SVM series is obtained by applying the boundary conditions of differential equations.

To validate the analytical solutions, differential equations of chapter 2 are solved numerically in chapter 3. For acoustic problem, a first harmonic boundary acceleration is applied to the boundary. The analytical and numerical solutions of this problem are juxtaposed and their error is presented. In electrical problem for an acoustic point source excitation, the problem is solved analytically and numerically. The electric potential distribution for both cases are presented. The relative error between two cases is given. Also the improvement in the average relative error as number of terms in SVM series increases is provided.

A sensitivity expression is derived for MAET in chapter 4 by utilizing the analytical solutions derived earlier. First the Fourier coefficients of electric potential on the boundary is related to the Fourier coefficients of acoustic boundary acceleration. Then by taking the fractional derivative of potential with respect to conductivity contrast, the sensitivity expression is obtained. The relations between the sensitivity and physical parameters of the object of interest are given. Finally, conformal mapping is utilized to obtain an expression for sensitivity of eccentric circle bodies.

In chapter 5, the tissue heating in MAET imaging method is investigated. Due to application of acoustic pressure and resultant Lorentz current the tissue temperature increases. Here the steady state heat distribution in the tissues is obtained. Then an acoustic excitation is applied for a second and the temperature increase in the tissues and the cooling process afterwards is demonstrated.

CHAPTER 2

ANALYTICAL SOLUTION OF MAET

In order to assess the performance of MAET we have obtained an analytical expression relating the acoustic excitation on the boundary to the measured electric potentials. To do so, first we expressed the Fourier series coefficient of particle velocities in terms of the Fourier coefficients of acoustic boundary acceleration by solving the Helmholtz equation for acoustic pressure. Then the differential equation for the electric potential is solved with particle velocity as a current source. This yields a relation between the acoustic boundary acceleration and the measured electric potential on the surface. The analytical solutions for the acoustic and electric problems are presented in following sections. Later in chapter 4, we relate the acoustic excitation to the electric potential by utilizing the analytical solutions in this chapter.

2.1 Acoustic Problem

In MAET imaging method, the tissue is excited by ultrasound. This excitation can be modeled as normal acceleration on the boundaries. Given such an excitation, the equation that the acoustic pressure obeys inside the domain Ω and its boundary condition are as follows (Fig. 1.1) [7]:

$$\begin{aligned}\nabla^2 p + k^2 p &= 0, \quad \text{in } \Omega \\ \mathbf{n} \cdot \nabla p &= \rho a_n, \quad \text{on } d\Omega\end{aligned}\tag{2.1}$$

where p (Pa) is the acoustic pressure, ρ (kg/m³) is the density of the medium and k

$(1/m)$ is the complex wave number which accounts for the acoustic attenuation inside the medium. Given an inward acceleration a_n (m/s^2) on the boundary and sound hard boundary on the remaining boundaries, a general expression based on Separation of Variables Method (SVM) is obtained for acoustic pressure p [20] (A homogeneous medium is assumed since acoustic properties of the breast tissue does not vary much).

By defining $p(r, \theta) = R(r)\Theta(\theta)$ and explicitly writing the Laplacian operator, the following expression is obtained for the Helmholtz equation:

$$\frac{d^2 R}{dr^2} \Theta + \frac{1}{r} \frac{dR}{dr} \Theta + \frac{1}{r^2} \frac{d^2 \Theta}{d\theta^2} R + k^2 R \Theta = 0 \quad (2.2)$$

Multiplying both sides with $r^2/(R\Theta)$ to decouple the variables, the updated equation is:

$$\frac{r^2}{R} \frac{d^2 R}{dr^2} + \frac{r}{R} \frac{dR}{dr} + k^2 r^2 + \frac{1}{\Theta} \frac{d^2 \Theta}{d\theta^2} = 0 \quad (2.3)$$

The solution to the angular component of acoustic pressure must be periodic. That is:

$$\frac{1}{\Theta} \frac{d^2 \Theta}{d\theta^2} = -m^2 \quad (2.4)$$

where m is a non-negative integer. The eigenfunction satisfying said conditions are $\{\cos(m\theta), \sin(m\theta)\}$ for real functions and $\{e^{jm\theta}, e^{-jm\theta}\}$ for complex functions. The boundary conditions of (2.1) determines the eigenfunction set. For real valued acoustic boundary condition both sets span the function space. Whereas for a complex valued acoustic boundary condition, exponential functions are the only eigenfunction set which can decompose the angular potential distribution. For such a case the general solution is given as:

$$\Theta(\theta) = A_m e^{jm\theta} + B_m e^{-jm\theta} \quad (2.5)$$

Consequently, the differential equation for the radial component is evaluated as:

$$\frac{r^2}{R} \frac{d^2 R}{dr^2} + \frac{r}{R} \frac{dR}{dr} + k^2 r^2 = m^2 \quad (2.6)$$

The solution to the above equation are Bessel functions of the first and second kind. The general solution for the radial component is:

$$R(r) = C_m J_m(kr) + D_m Y_m(kr) \quad (2.7)$$

Substituting (2.5) and (2.7) in $p(r, \theta) = R(r)\Theta(\theta)$, the general expression for acoustic pressure is obtained:

$$p(r, \theta) = \sum_{m=0}^{\infty} (A_m e^{jm\theta} + B_m e^{-jm\theta}) (C_m J_m(kr) + D_m Y_m(kr)) \quad (2.8)$$

Here A_m, B_m, C_m and D_m are the series expansion coefficients. $J_m(\cdot)$ and $Y_m(\cdot)$ are the Bessel functions of the first and second kinds. For a homogeneous circular object, $Y_m(\cdot)$ is not regular at origin, so its coefficient is set to zero.

$$p(r, \theta) = \sum_{m=0}^{\infty} (A_m e^{jm\theta} + B_m e^{-jm\theta}) J_m(kr) \quad (2.9)$$

The coefficients A_m and B_m are found from boundary condition of equation (2.1):

$$\mathbf{n} \cdot \left(\frac{dp}{dr} \mathbf{a}_r + \frac{1}{r} \frac{dp}{d\theta} \mathbf{a}_\theta \right) = \rho a_n \quad (2.10)$$

For a two dimensional concentric geometry given in Fig. 1.1, $\mathbf{n} = \mathbf{a}_r$. Taking the derivative of acoustic pressure with respect to r and using the orthogonality of complex exponentials in (2.10), coefficients A_m and B_m are obtained as:

$$A_m = \frac{\rho}{\pi (J_{m-1}(kR_2) - J_{m+1}(kR_2))} \int_0^{2\pi} a_n e^{-jm\theta} d\theta \quad (2.11)$$

$$B_m = \frac{\rho}{\pi (J_{m-1}(kR_2) - J_{m+1}(kR_2))} \int_0^{2\pi} a_n e^{jm\theta} d\theta \quad (2.12)$$

2.2 Electrical Problem

The electromagnetic forward problem of MAET is in the form of coupled differential equations. To solve the forward problem, both electric potential and magnetic vector potential must be calculated. In [7], the electrical and magnetic differential equations are decoupled assuming that the displacement currents and inductive currents can be ignored. Also at frequency of 1 MHz, the propagation effect is negligible. Consequently, adopting the quasi-static approximation, by setting the divergence of total current density to zero, a differential equation for the electric potential is obtained. The equation and its boundary condition are as follows:

$$\nabla \cdot (\sigma \nabla \phi) = \nabla \cdot (\mathbf{J}_{Lorentz}), \quad \text{in } \Omega \quad (2.13)$$

$$\frac{\partial \phi}{\partial n} = \mathbf{n} \cdot (\mathbf{v} \times \mathbf{B}_0), \quad \text{in } d\Omega$$

where σ (S/m) is electrical conductivity, ϕ (V) is electric potential, $\mathbf{J}_{Lorentz}$ (A/m²) is Lorentz current density, \mathbf{v} (m/s) is particle velocity and \mathbf{B}_0 (T) is the static magnetic field density. The current density due to Lorentz field is expressed as $\mathbf{J}_{Lorentz} = \sigma \mathbf{v} \times \mathbf{B}_0$.

Since the acoustic source is on the boundary, the divergence of \mathbf{v} is zero inside the body. Then the right hand side of (2.13) can be written as $\nabla \sigma \cdot (\mathbf{v} \times \mathbf{B}_0)$. The conductivity gradient and hence divergence of Lorentz current is zero for regions with homogeneous conductivity. For the geometry in Fig. 1.1, equation (2.13) and its boundary condition can be written as [7]:

$$\nabla \cdot (\sigma \nabla \phi_1) = 0, \quad 0 < r < R_1 \quad (2.14)$$

$$\nabla \cdot (\sigma \nabla \phi_2) = 0, \quad R_1 < r < R_2$$

$$\frac{\partial \phi_2}{\partial r} = \mathbf{a}_r \cdot (\mathbf{v} \times \mathbf{B}_0), \quad \text{on } R_2$$

On $r = R_1$, the electric potential should satisfy the following continuity equations:

$$\sigma_2 \frac{\partial \phi_2}{\partial r} - \sigma_1 \frac{\partial \phi_1}{\partial r} = (\sigma_2 - \sigma_1) \mathbf{a}_r \cdot (\mathbf{v} \times \mathbf{B}_0), \quad \text{on } R_1$$

$$\phi_2 = \phi_1, \quad \text{on } R_1$$

Continuity of electric potential and normal component of currents is assumed on the interface at $r = R_1$. Implementing SVM reduces the Laplace equation to eigenvalue problems for angular and radial components of electric potential.

$$\phi(r, \theta) = R(r)\Theta(\theta) \quad (2.15)$$

Similar to the acoustic problem, the angular eigenfunctions are either $\{\cos(m\theta), \sin(m\theta)\}$ or $\{e^{jm\theta}, e^{-jm\theta}\}$. The velocity distribution on the boundaries determines whether real or complex eigenfunctions are required to represent the distribution. Then the radial component of electric potential satisfies following equation:

$$\frac{d^2 R}{dr^2} + \left(\frac{1}{r} + \frac{d \ln(\sigma)}{dr} \right) \frac{dR}{dr} - \frac{m^2}{r^2} R = 0 \quad (2.16)$$

Here m is a positive integer. The eigenfunctions are $\{1, \ln r, r^m, r^{-m}\}$ for radial component. Linear combination of the eigenfunctions also satisfies the Laplace equation. The general solution for the Laplace equation in the 2D concentric body is [16]:

$$\phi(r, \theta) = A + B \ln r + \sum_{m=1}^{\infty} (a_m r^m + b_m r^{-m}) e^{jm\theta} + (c_m r^m + d_m r^{-m}) e^{-jm\theta} \quad (2.17)$$

The equation above is valid for both regions given in (2.14). For the inner region of radius R_1 , the electric potential must be finite. To satisfy this requirement the coefficient for r^{-m} is set to zero. Due to Neumann boundary conditions, the solution for electric potential is determined up to a constant. Applying the boundary conditions of (2.14), the first two terms in (2.17) for both inner and outer regions can be set to zero. Then the electric potentials can be expressed as follows:

$$\phi_1(r, \theta) = \sum_{m=1}^{\infty} r^m (e_m e^{jm\theta} + f_m e^{-jm\theta}), \quad 0 < r < R_1 \quad (2.18)$$

$$\phi_2(r, \theta) = \sum_{m=1}^{\infty} (a_m r^m + b_m r^{-m}) e^{jm\theta} + (c_m r^m + d_m r^{-m}) e^{-jm\theta}, \quad R_1 < r < R_2 \quad (2.19)$$

Using orthogonality principles of complex exponentials and boundary conditions, the coefficients a_m , b_m and e_m of the series expansion can be obtained by solving the following equations:

$$\sigma_2(a_m m R_2^{m-1} - b_m m R_2^{-m-1}) = \frac{1}{2\pi} \int_0^{2\pi} \nabla \sigma \cdot (\mathbf{v} \times \mathbf{B}) e^{-jm\theta} d\theta \quad (2.20)$$

$$\sigma_2(a_m m R_1^{m-1} - b_m m R_1^{-m-1}) - \sigma_1(e_m m R_1^{m-1}) = \int_0^{2\pi} \nabla \sigma \cdot (\mathbf{v} \times \mathbf{B}) e^{-jm\theta} d\theta \quad (2.21)$$

$$a_m R_1^m + b_m R_1^{-m} = e_m R_1^m \quad (2.22)$$

The other three coefficients c_m , d_m and f_m , can be obtained similarly by applying the orthogonality principle:

$$\sigma_2(c_m m R_2^{m-1} - d_m m R_2^{-m-1}) = \frac{1}{2\pi} \int_0^{2\pi} \nabla \sigma \cdot (\mathbf{v} \times \mathbf{B}) e^{jm\theta} d\theta \quad (2.23)$$

$$\sigma_2(c_m m R_1^{m-1} - d_m m R_1^{-m-1}) - \sigma_1(f_m m R_1^{m-1}) = \int_0^{2\pi} \nabla \sigma \cdot (\mathbf{v} \times \mathbf{B}) e^{jm\theta} d\theta \quad (2.24)$$

$$c_m R_1^m + d_m R_1^{-m} = f_m R_1^m \quad (2.25)$$

CHAPTER 3

ACCURACY OF THE ANALYTIC SOLUTIONS

In this chapter, we investigate the MAET method numerically for simplified geometries. First the analytical solutions developed in the previous chapter are tested by solving the potential distribution numerically and analytically. For the acoustic case, a simple harmonic boundary condition is applied to a homogeneous circular object. The problem is solved in COMSOL and is compared to the analytical solution of the same problem. For the electrical problem, an acoustic point source is placed above the body. The electric potential due to induced Lorentz currents is calculated using COMSOL. Here the Lorentz current on the boundaries can be decomposed to their harmonic components. The analytical solution of the same excitation is obtained and compared to the numerical solution. The relative error between the two calculations are presented.

3.1 Acoustic Problem

To investigate the accuracy of the analytical solution in chapter 2, we solve the equation (2.1) numerically. For simplicity, the acoustic excitation on the outer boundary is set $a_n = A \cos(\theta)$, where A is the amplitude of excitation. Given this excitation inside a circle of radius R_2 , the analytical solution can be written as:

$$p(r, \theta) = \frac{2A\rho \cos(\theta)}{k(J_0(kR_2) - J_2(kR_2))} J_1(kr) \quad (3.1)$$

We perform the simulation for a circular region ($R_2 = 5$ cm) with the acoustic prop-

erties of the gland tissue. The speed of sound in the gland tissue is 1505 m/s at the operation frequency of 1 MHz. The resultant acoustic wavelength is 1.505 mm. To obtain an accurate simulation result, the domain is meshed with 0.1 mm triangular elements. It contains 1,694,806 nodes and 3,386,466 elements. The acoustic absorption coefficient of gland tissue at this frequency is 8.635 Np/m. The boundary acceleration is set as 10^5 m/s².

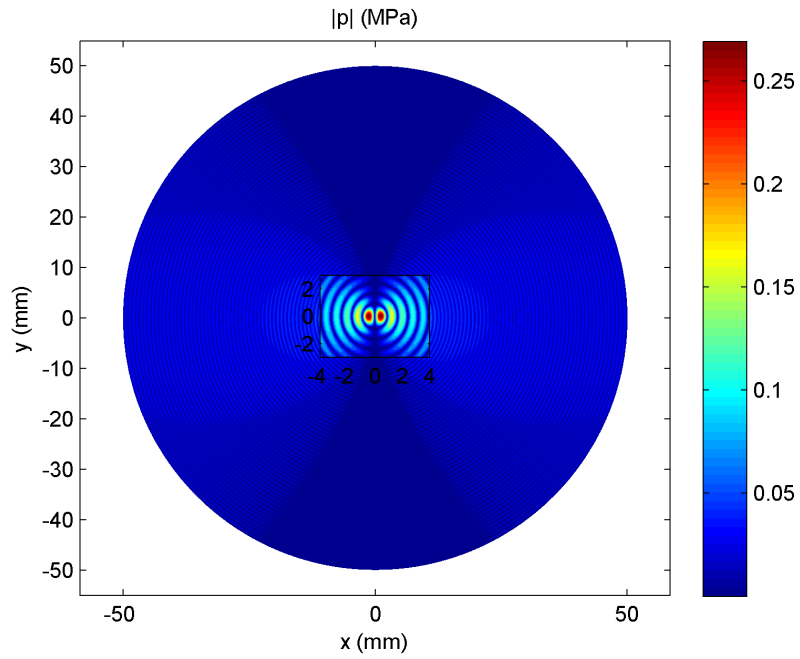
We obtained the analytical solution for the same parameters by evaluating the acoustic pressure at each mesh node analytically from (3.1). The two filled contour plots are given side by side in Fig. 3.1. To better demonstrated the high acoustic pressure close to the origin, zoomed in contour plots are added to the figure.

To analyze the error between analytical and numerical solutions, we calculate the relative error in absolute value of these solutions for each point on the FEM mesh. Since both solutions are complex, the absolute value of the phase difference between the solutions is also evaluated. These equations are given as:

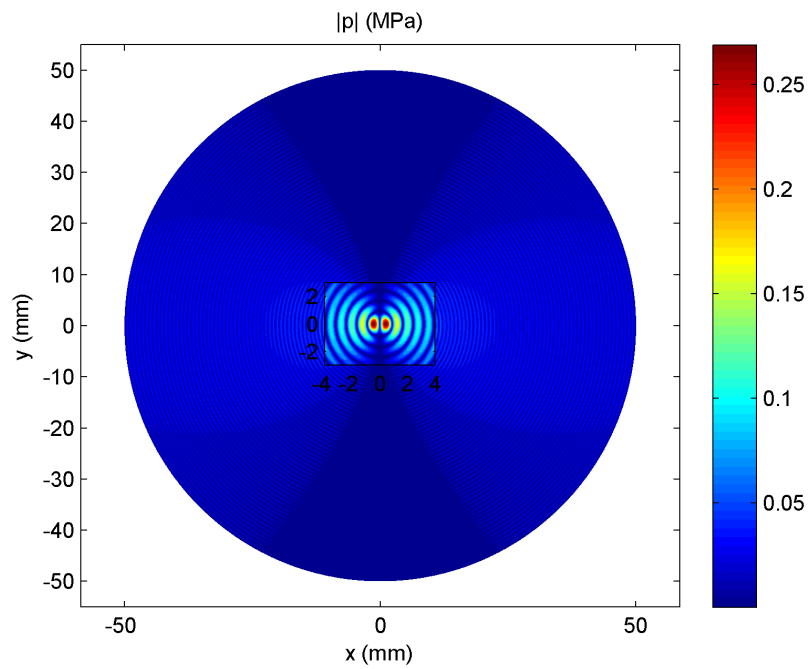
$$e_{magnitude} = \frac{||p_{analytical}| - |p_{numerical}||}{|p_{analytical}|} \quad (3.2)$$

$$e_{phase} = |arg(p_{analytical}) - arg(p_{numerical})| \quad (3.3)$$

Fig. 3.2 contains the location of the points with relative errors greater than 10 % and phase differences greater than 5°. It is observed that the points with greater error are the zero acoustic pressure points. The numerical solution does have practically zero values, however analytical solution is orders of magnitudes less than the numerical one. Assuming the analytical solution as the reference, the relative errors for such points are large in value. The average value for the relative error among 1,694,806 points is 0.064 %. For the phase difference, the average error in phase is 0.24°.



(a) Analytical



(b) Numerical

Figure 3.1: (a) The analytical and (b) numerical acoustic pressure distributions inside a homogeneous circle of radius $R_2 = 5$ cm. First harmonic boundary acceleration is applied and acoustic properties of the gland tissue are assumed. The acoustic pressure distribution close to the origin is magnified to enhance its details.

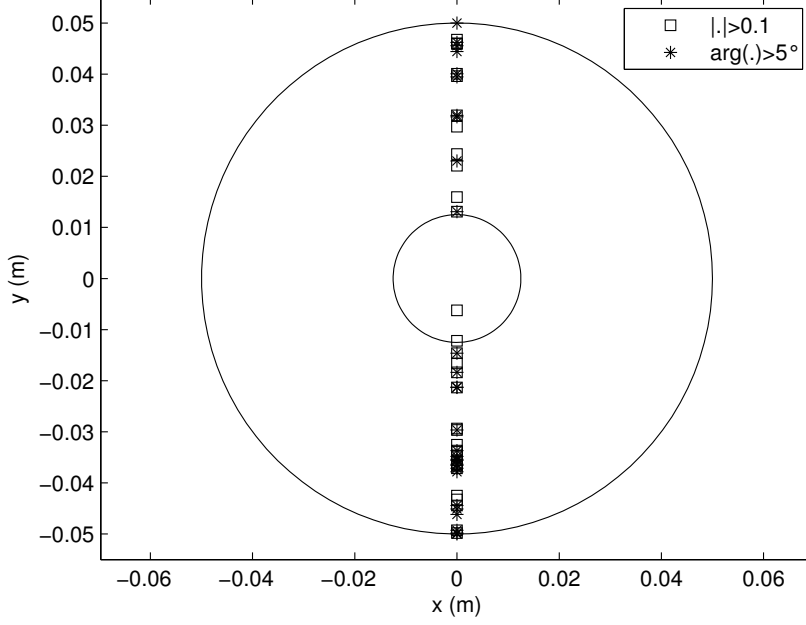


Figure 3.2: Location of points with relative error (acoustic pressure's magnitude) greater than 10 % (32 points) and a phase difference greater than 5° (29 points).

3.2 Electrical Problem

Now that we presented the accuracy of acoustic solution, here we take a different approach for the electrical problem. Here the body (medium) is excited by an acoustic point source for which a closed analytical expression exist. The point source is placed above the body (Fig. 3.3). As a result, the current distribution on boundaries encompasses wide harmonic range. It is assumed that there is no acoustic reflection from the boundaries. The flow rate of acoustic source is Q (m^2/s). The acoustic pressure distribution for a medium with density ρ (kg/m^3) and velocity c (m/s) satisfies the following equation (An acoustically homogeneous media is assumed) [21]:

$$\nabla^2 p + k^2 p = -\rho Q(\mathbf{r})\delta(\mathbf{r} - \mathbf{r}_s) \quad (3.4)$$

here \mathbf{r} is the field point and \mathbf{r}_s is the source point.

$$p(R) = \frac{\omega_a \rho Q}{4} H_0^2(kR) \quad (3.5)$$

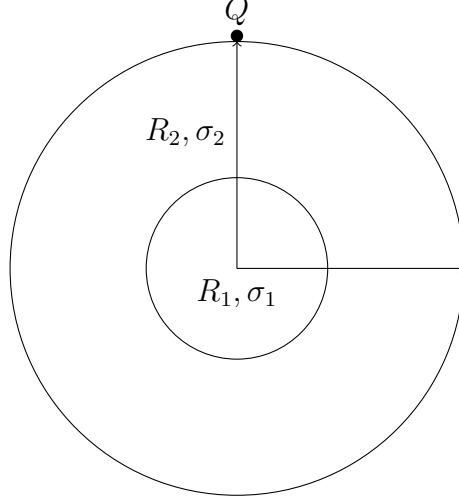


Figure 3.3: Concentric circle geometry with an acoustic point source Q .

where $R = \sqrt{r^2 + r_s^2 - 2rr_s \cos(\theta - \theta_s)}$ is the distance of the source (r_s, θ_s) to any point (r, θ) , $H_0^2(\cdot)$ is the zero order Hankel function of the second kind and ω_a is equal to kc . Then the particle velocity can be calculated from the pressure distribution [22]:

$$\mathbf{v} = \frac{j}{\omega_a \rho} \nabla p \quad (3.6)$$

The particle velocity (\mathbf{v}) which is generated by the acoustic propagation, gives rise to Lorentz current under a static magnetic field \mathbf{B}_0 .

The differential equation for the electrical problem of MAET is described by equation (2.13) and its boundary condition. In COMSOL Multiphysics, the equation is solved in AC/DC module. Due to application of Neumann boundary condition, the problem is not yet uniquely defined. To ensure convergence of the solution in analytical and numerical problems, electric potential is set to zero at the center of concentric circles. This makes the problem solution unique. For the comparison of the analytical and numerical results, relative errors are calculated for all mesh nodes with following equations ($|\cdot|$ is the magnitude of \cdot):

$$e_{magnitide} = \frac{||\phi_{analytical}| - |\phi_{numerical}||}{|\phi_{analytical}|} \quad (3.7)$$

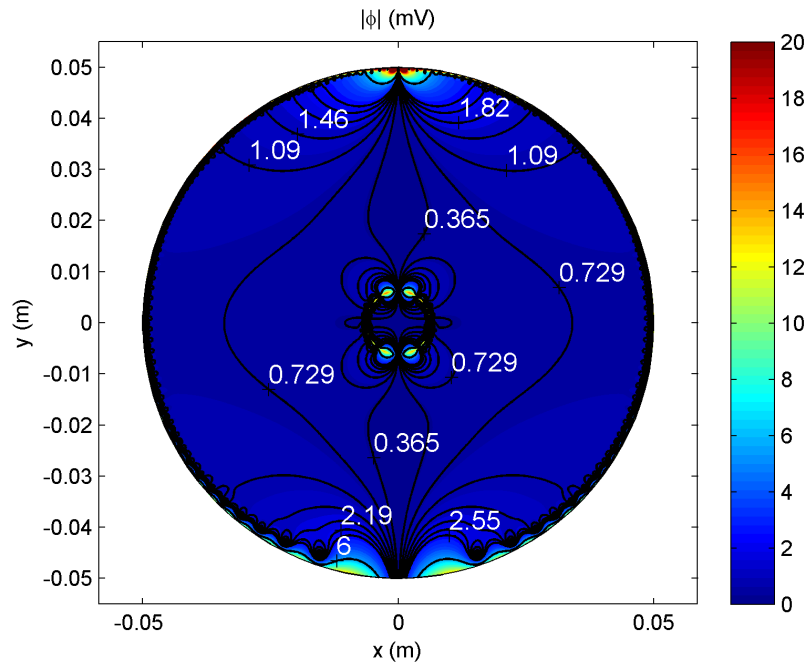
$$e_{phase} = |arg(\phi_{analytical}) - arg(\phi_{numerical})| \quad (3.8)$$

Analytical and numerical results of the forward problem of MAET are presented and compared in magnitude for two different inner circle (Tumor) radius. In the first configuration, the point source is excited by 1 MHz sinusoidal wave. The model consists of a circle of radius 6.25 mm with conductivity 2 S/m and an annulus of radius 5 cm with conductivity 0.2 S/m. The model is acoustically homogeneous with acoustic propagation speed of 1520 m/s and density of 980 kg/m³ (properties of fat tissue). The flow rate of acoustic point source is chosen as 1 m²/s and the magnetic flux density which is perpendicular to plane of Fig. 1.1, is 1 T. In COMSOL, the domain is discretized by triangular mesh elements with maximum length of one tenth of wavelength ($\lambda/10$). The model consists of 1, 041, 390 elements and 521, 744 nodes. The relative errors are calculated with equations (3.7) and (3.8).

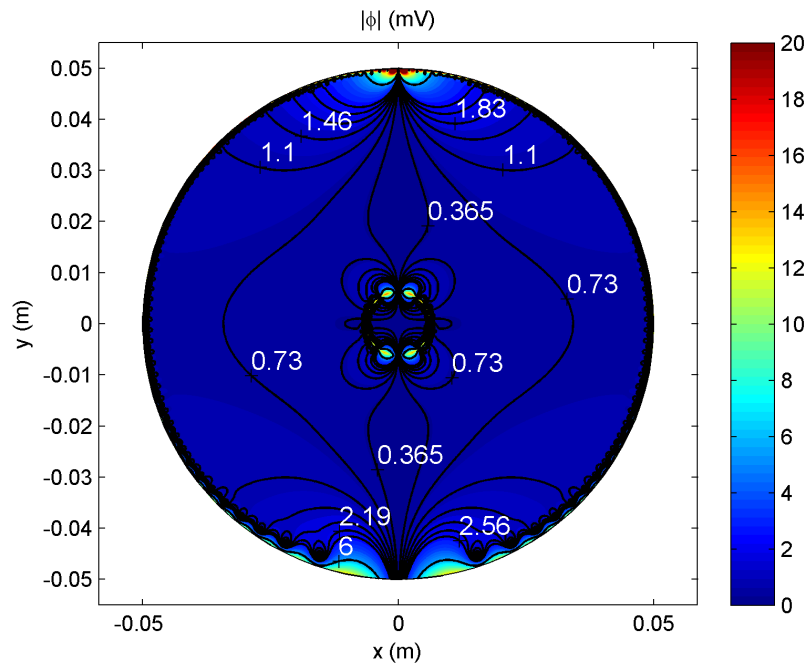
The analytical and numerical solutions of electric potential distributions for the first case are given in Fig. 3.4. The accuracy of the numerical method is dependent on the mesh quality and number of mesh elements. As seen in Fig. 3.4(a) and 3.4(b), the magnitude of electric potential is maximum close to acoustic source.

To better demonstrate the differences between these solutions, the locations of points with high relative error, in absolute value and phase difference, are presented in Fig. 3.5. The nodes with relative error above 5 % are calculated and their locations are plotted on the geometry. The nodes with a phase difference greater than 2° are also marked by an asterisk sign. It is observed that the highest errors are in the regions with sharp changes in the electric potential. In Fig. 3.5, only 7 points out of 521, 744 points have error higher than 5 %. Also average of relative error in magnitude for 521, 744 points is 0.14 %. The average value for phase difference of all points is 0.67°. In calculation of relative error, 4 points along the $x = 0$ line are discarded. The electric potential is zero for these points. However since the analytical electric potential's magnitude is orders of magnitude less than the numerical solution's magnitude, the relative error becomes too large.

The separation of variables method represents the solution by a series expansion. Here we investigate the improvement in analytical solution by adding new term to



(a) Analytical



(b) Numerical

Figure 3.4: (a) The analytical and (b) numerical magnitude of electric potential in 2D concentric circles. The potential is maximum close to acoustic source. The radius of the concentric inhomogeneity is 6.25 mm.

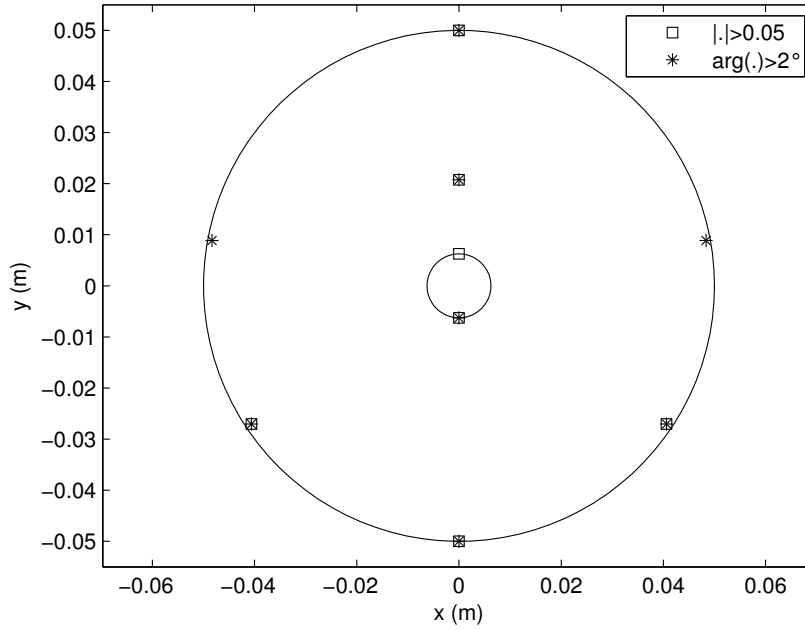


Figure 3.5: Location of points with relative error (electric potential’s magnitude) greater than 5 % and phase difference of greater than 2° . The other points of FEM mesh have lower errors in absolute value and phase.

the solution. In Fig. 3.6, the decrease in absolute value of the relative error is visible as more terms are added to the series expansion. The average value of relative error is above 250 % when the electric potential distribution consists of single term. As more terms are added to electric potential, the average error reduces to 0.14 %. Since the current distribution has not any component above the 220th harmonic, additional terms has no effect on the accuracy of the representation.

The second model consists of a circle of radius 3.125 mm with conductivity 2 S/m and an annulus of radius 5 cm with conductivity 0.2 S/m. The other parameters are the same as in the first case. In COMSOL, the domain is discretized by triangular mesh elements with the same maximum length as in the first case. The model consists of 1, 457, 268 elements and 729, 669 nodes. The relative errors are calculated with (3.7) and (3.8).

The analytical and numerical solutions of electric potential distributions for the second case are given in Fig. 3.7. Similar to the first case, the magnitude of electric potential is maximum close to acoustic source in Fig. 3.7(a) and 3.7(b).

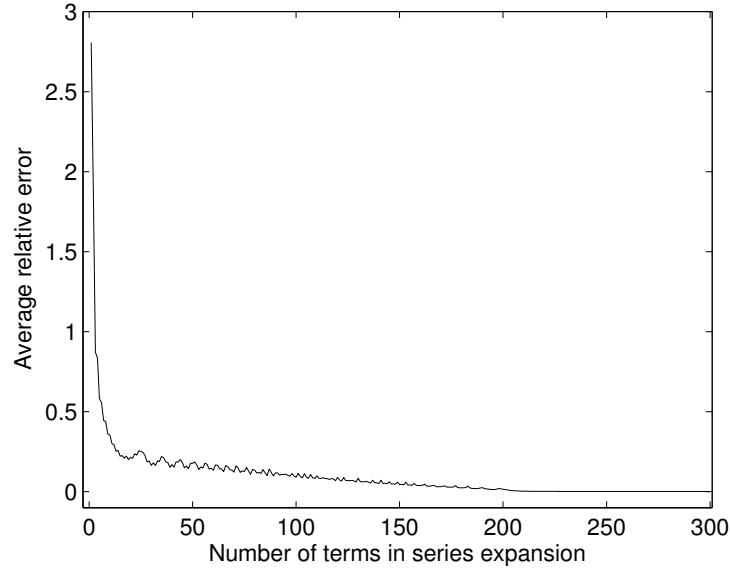
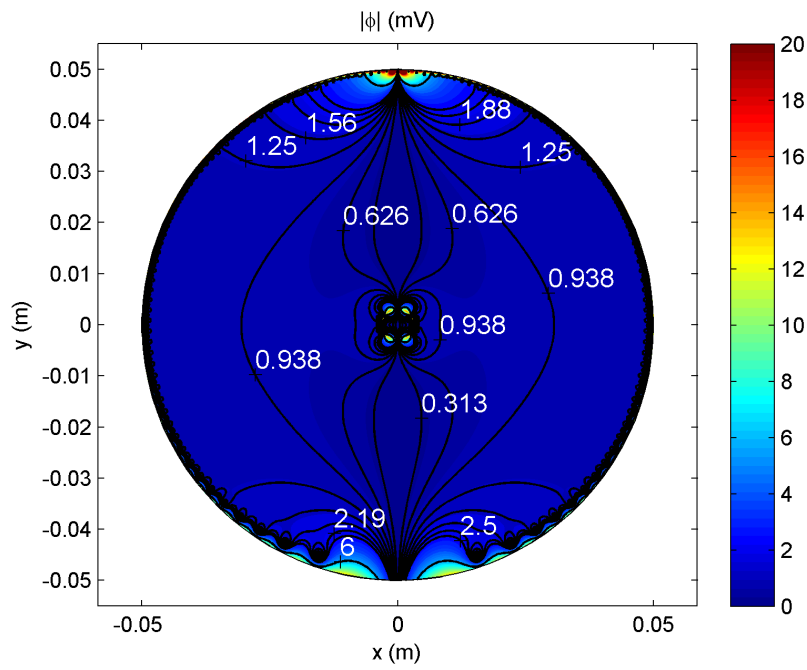
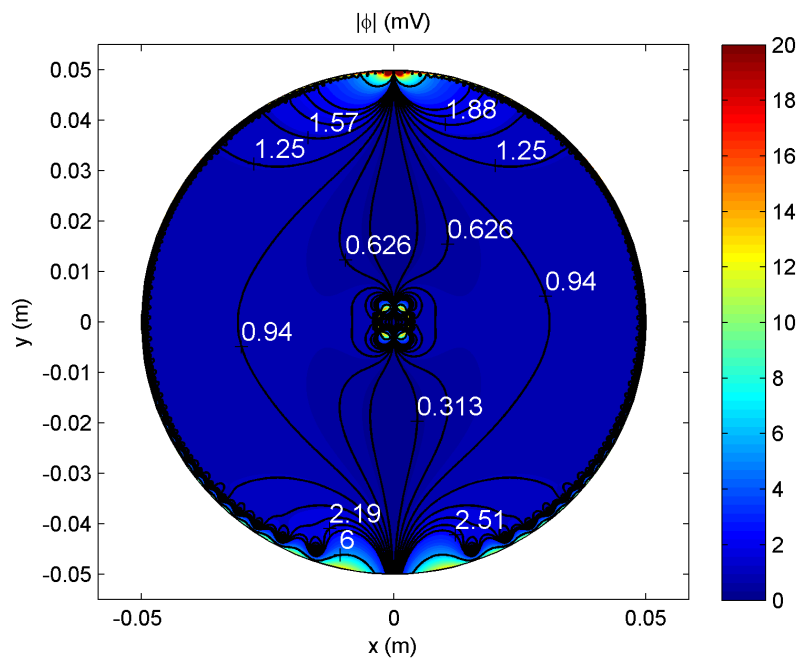


Figure 3.6: The average relative error in absolute value of electric potential between the analytical and numerical solutions as a function of number of terms in series expansion ($R_1 = 6.25$ mm).

To assess the accuracy in solutions, the locations of points with high relative error, in absolute value and phase difference, are presented in Fig. 3.8. Similar to the first case, here the highest errors are in the regions where there are sharp changes in the electric potential. In Fig. 3.5, only 9 points out of 729,669 points have error higher than 5%. Also average of relative error in magnitude for 521,744 points is 0.041%. The average value for phase difference of all points is 0.64° . Similar to the first case, in calculation of relative error, 4 points along the $x = 0$ line are discarded. The electric potential is zero for these points. However since the electric potentials magnitude is orders of magnitude less than the numerical solutions magnitude, the relative error becomes too large. Here there are more points with high relative error compared to the first case. However the average relative error in absolute value and phase is lower. The reason for this behaviour is the smaller tumor radius in the second case. The mesh generator in COMSOL meshes this region, with a low error in absolute value, finer than the first case. So the average values for the second case are lower.



(a) Analytical



(b) Numerical

Figure 3.7: (a) The analytical and (b) numerical magnitude of electric potential in 2D concentric circles. The potential is maximum close to acoustic source. The radius of the concentric inhomogeneity is 3.125 mm.

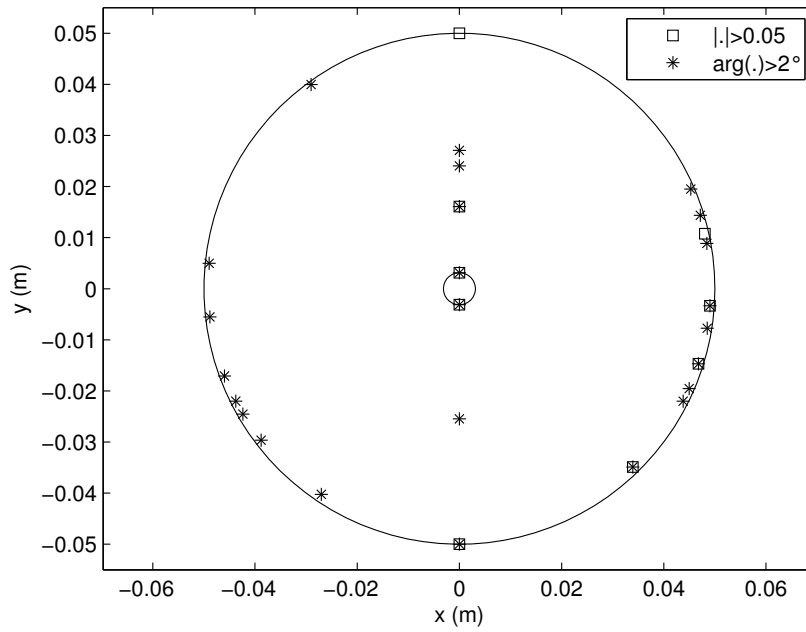


Figure 3.8: Location of points with relative error (electric potential's magnitude) greater than 5 % and phase difference of greater than 2° . The other points of FEM mesh have lower errors in absolute value and phase.

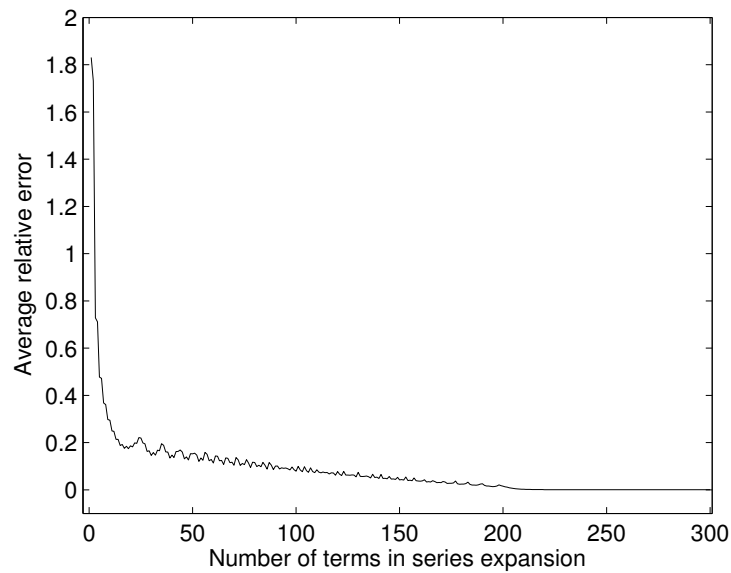


Figure 3.9: The average relative error in absolute value of electric potential between the analytical and numerical solutions as a function of number of terms in series expansion ($R_1 = 3.125$ mm).

CHAPTER 4

SENSITIVITY ANALYSIS FOR MAET

After revealing the accuracy of analytical solutions in chapter 2, in this chapter we drive an expression for the sensitivity of MAET, which relates the changes in conductivity contrast to changes in electric potentials. The sensitivity expression is a function of resolution, conductivity contrast, body's outer radius and acoustic wave number. To do so, first we represent the Lorentz currents on the inner and outer boundaries in terms of the acoustic boundary acceleration. Then through the boundary equations of electric potential, we relate the Fourier series coefficients of electric potential on outer boundary, to the Lorentz current densities inside the body. As a result, the electric potential is related to the acoustic boundary acceleration. The pair-wise relations between sensitivity and the systems parameters are demonstrated for different cases. Conformal mapping is implemented to describe the behaviour of MAET for eccentric circles. The sensitivity expression of MAET is compared to EIT's sensitivity for different boundary accelerations. Finally, a sensitivity expression for arbitrary boundary excitations is derived.

4.1 Deriving the Sensitivity Expression

We derived the analytical solutions for acoustic and electrical problems of MAET in chapter 2. Here we use those equations to relate the Fourier series of acoustic boundary acceleration to the surface electric potential. Let a_n on S be represented as a Fourier series as follows:

$$a_n = \sum_{m=0}^{\infty} \gamma_m e^{jm\theta} + \delta_m e^{-jm\theta} \quad (4.1)$$

The boundary condition of equation (2.1), relates the acoustic pressure p to the boundary acceleration, a_n . Given the series expansion of acoustic pressure in (2.9) and (4.1), the series coefficients of p , A_m and a_n , γ_m are related as:

$$A_m = \frac{2\rho\gamma_m}{k(J_{m-1}(kR_2) - J_{m+1}(kR_2))} \quad (4.2)$$

For a concentric circle geometry of Fig. 1.1, only the radial component of $\mathbf{J}_{\text{Lorentz}}$ changes the electric potential. Noting that $\mathbf{B}_0 = B_0 \mathbf{a}_z$, $\mathbf{J}_{\text{Lorentz}} = \sigma \mathbf{v} \times \mathbf{B}_0$ and $\mathbf{v} = j\nabla p / \rho\omega$ the radial component of Lorentz current is represented as:

$$J_{\text{Lorentz}_r} = \sigma v_\theta B_0 = \frac{j\sigma B_0}{\rho\omega} \frac{1}{r} \frac{\partial p}{\partial \theta} \quad (4.3)$$

The Fourier series of radial component of Lorentz current on R_1 and R_2 are:

$$J_{R_1} = \sum_{m=0}^{\infty} \zeta_m^1 e^{jm\theta} + \eta_m^1 e^{-jm\theta} \quad (4.4)$$

$$J_{R_2} = \sum_{m=0}^{\infty} \zeta_m^2 e^{jm\theta} + \eta_m^2 e^{-jm\theta} \quad (4.5)$$

Then ζ_m^1 and ζ_m^2 can be related to γ_m using relations (4.2) and (4.3) as follows:

$$\zeta_m^1 = \frac{2m\sigma B_0 J_m(kR_1) \gamma_m}{\omega R_1 k (J_{m-1}(kR_2) - J_{m+1}(kR_2))} \quad (4.6)$$

$$\zeta_m^2 = \frac{2m\sigma B_0 J_m(kR_2) \gamma_m}{\omega R_2 k (J_{m-1}(kR_2) - J_{m+1}(kR_2))} \quad (4.7)$$

Now that the Fourier series of the Lorentz current is linked to the acoustic boundary acceleration, the mentioned Fourier series is added to the electromagnetic problem of the MAET. The electric potential in the forward problem of MAET is given in equation (2.14). Driving Point Impedance relates the current sources on R_1 and R_2 to the electric potential on R_2 . For MAET, it is defined as:

$$z_{mm} = \frac{a_m R_2^m + b_m R_2^{-m}}{\gamma_m} = -\frac{c_m R_2^m + d_m R_2^{-m}}{\delta_m} \quad (4.8)$$

By implementing boundary conditions of (2.14), i.e., continuity of normal component of current density and continuity of the electric potential across boundaries, Fourier coefficients of electric potential and current density are obtained as:

$$\sigma_2(a_m m R_2^{m-1} - b_m m R_2^{-m-1}) = \zeta_m^1 \quad (4.9)$$

$$\sigma_2(a_m m R_1^{m-1} - b_m m R_1^{-m-1}) - \sigma_1(e_m m R_1^{m-1}) = \zeta_m^2 \quad (4.10)$$

$$a_m R_1^m + b_m R_1^{-m} = e_m R_1^m \quad (4.11)$$

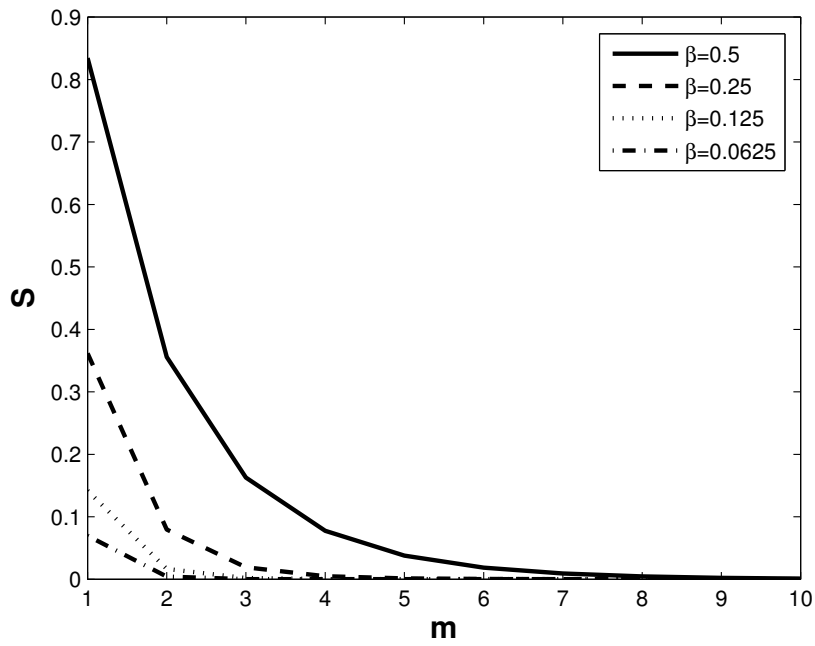
Using (4.9), (4.10) and (4.11), an expression for equation (4.8) is calculated as:

$$z_{mm} = \frac{-2B_0 [J_m(kR_2)((\alpha - 1)\beta^m - (1 + \alpha)\beta^{-m}) + 2(1 - \alpha)J_m(kR_1)]}{\omega k (J_{m-1}(kR_2) - J_{m+1}(kR_2)) [(1 - \alpha)\beta^m - (1 + \alpha)\beta^{-m}]} \quad (4.12)$$

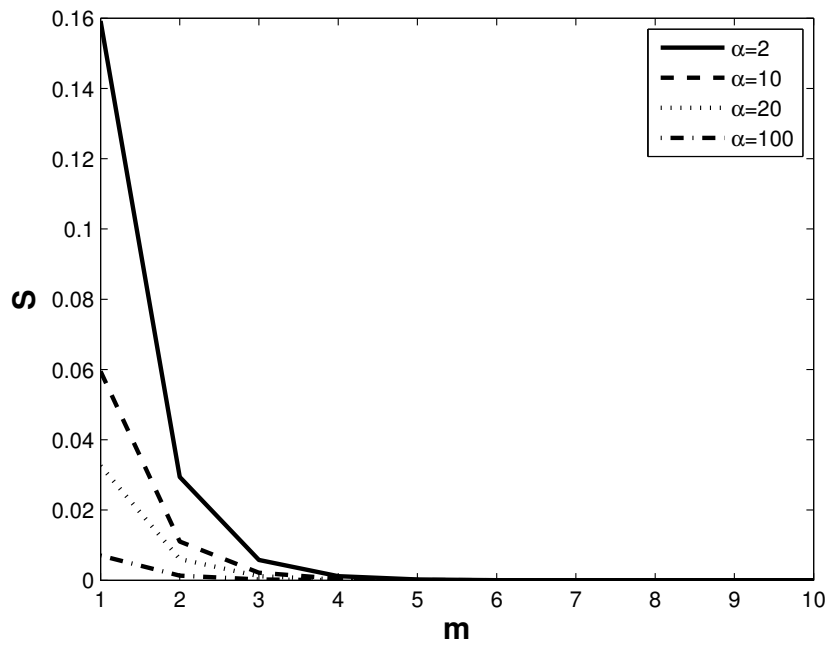
In equation (4.12), $\beta = R_1/R_2$ is the resolution and $\alpha = \sigma_1/\sigma_2$ is the conductivity contrast of MAET. Representing electric potential with respect to inner sources and taking its derivative with respect to conductivity contrast, sensitivity expression is obtained. Fixing the outer radius R_2 , R_1 can be represented as βR_2 . Then, the sensitivity expression is given as ($S_m(\alpha, \beta, k, R_2) = (d\phi/\phi)(\alpha/d\alpha)$):

$$S_m = \frac{4\alpha(\beta^{-m} \frac{J_m(k\beta R_2)}{J_m(kR_2)} - 1)}{\frac{J_m(k\beta R_2)}{J_m(kR_2)} [2(1 - \alpha)^2 \beta^m + 2(\alpha^2 - 1)\beta^{-m}] + (1 + \alpha)^2 \beta^{-2m} - (1 - \alpha)^2 \beta^{2m}} \quad (4.13)$$

For $\alpha = 1$, $R_2 = 5$ cm and acoustic properties of the gland tissue, the sensitivity expression of (4.13) is plotted as a function of m for different β values (Fig. 4.1(a)). Also for $\beta = 0.2$, the sensitivity of the gland tissue is given as a function of m for different α values (Fig. 4.1(b)).



(a)



(b)

Figure 4.1: The sensitivity of MAET as a function of m for different resolution values in (a) and different conductivity contrast values in (b).

It is observed that the sensitivity of MAET is greatest for $m = 1$ independent of resolution and conductivity contrast. Also for a fixed m , the fractional change in electric potential is greatest for $\beta = 0.5$ and $\alpha = 2$ in Fig. 4.1(a) and Fig. 4.1(b) respectively. Since the greatest change in fractional voltage occurs when $m = 1$, we derive the relations between the sensitivity and the other parameters for this case.

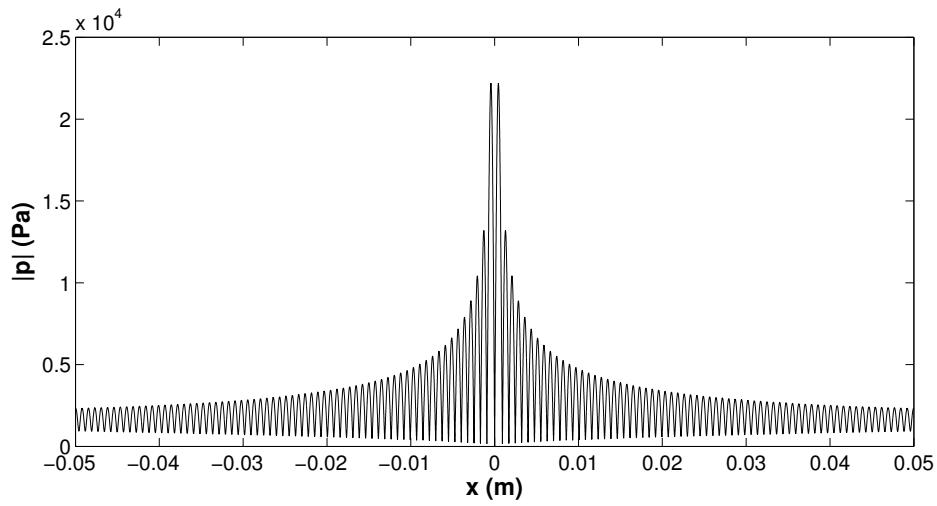
4.2 Pair-wise Relations

Before giving the pair-wise relations for $m = 1$, it is important to visualize the pressure and velocity distribution for such a case. The absolute value of the acoustic pressure p and θ component of velocity are circularly symmetric. The one dimensional absolute value distribution of these parameters are given along the x-axis. These distributions are obtained analytically. Note that with the definition of resolution given above $\beta = R_1/R_2$, the sensitivity to smaller resolutions corresponds to the sensitivity to smaller inhomogeneities.

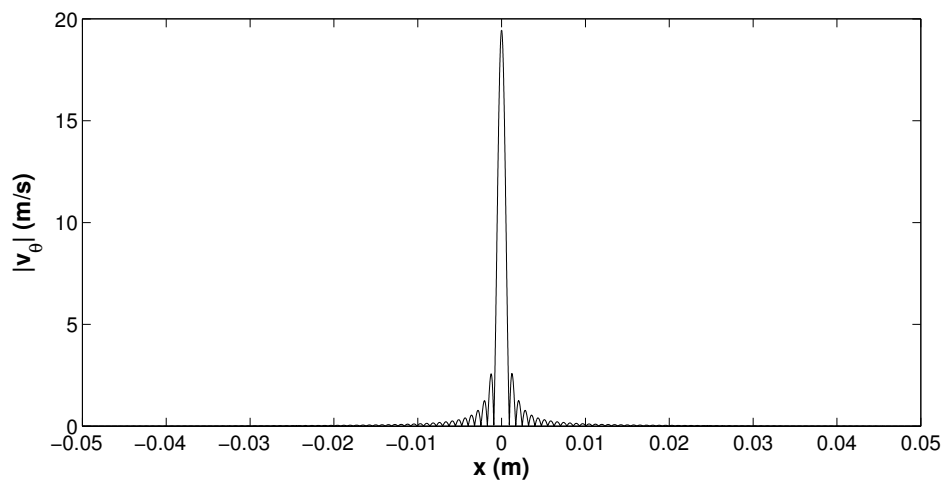
4.2.1 Sensitivity-Resolution

Seagar et al. [6] has presented pair-wise relations between S , α and β for applied current EIT. In this study, similar interrelations are obtained for MAET by adding acoustic properties of k and R_2 . To relate the two parameters of interest to each other, other parameters are fixed. First, the relation between sensitivity and resolution is investigated for different conductivity contrast values. The outer radius is $R_2 = 0.05$ m, acoustic attenuation is $a = 8.635$ Np/m, speed of sound is $c = 1520$ m/s, and frequency is $f = 1$ MHz. Due to characteristics of the Bessel function, the behavior of the sensitivity function is oscillatory for large arguments. This behaviour is due to the oscillatory nature of particle velocity in MAET and consequently the oscillatory behaviour of divergence of Lorentz current. To clarify this claim, the real and imaginary parts of divergence of the Lorentz current and sensitivity are plotted for $m = 1$. The outer radius is $R_2 = 5$ cm and the conductivity contrast is $\alpha = 1$. This comparison is demonstrated in Fig. 4.3.

As $\beta \rightarrow 0$, Bessel function of integer order can be written as [23]:

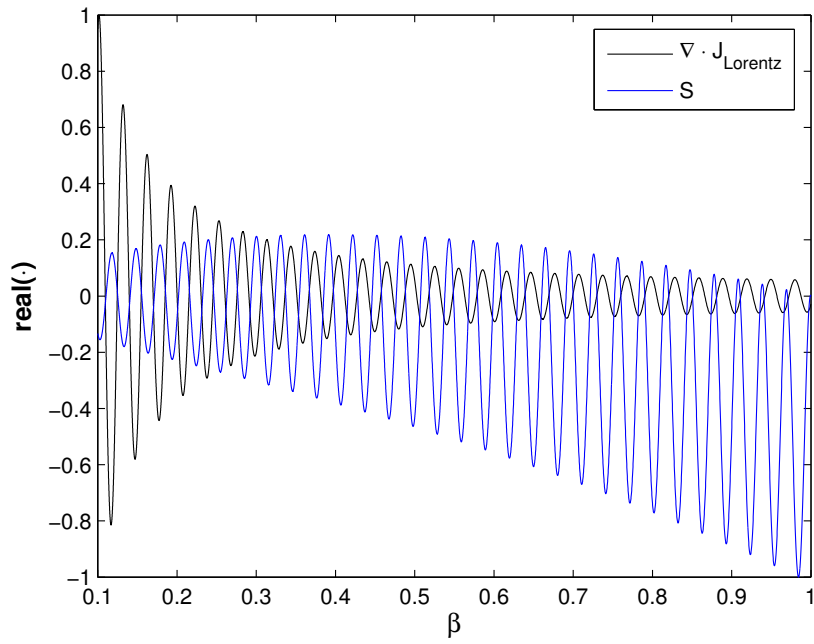


(a)

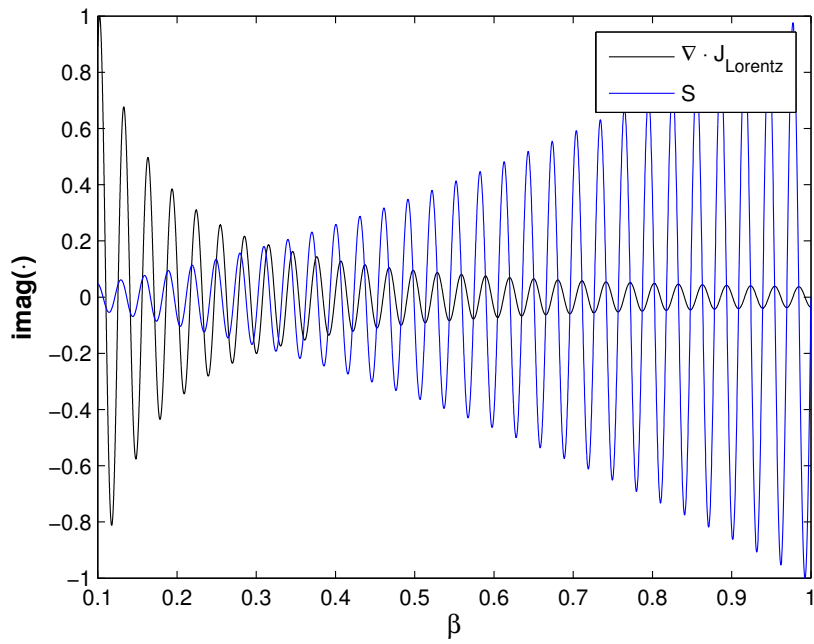


(b)

Figure 4.2: (a) The distribution of the absolute value of acoustic pressure and (b) the absolute value for θ component of acoustic velocity along the x axis. These distributions are radially symmetric.



(a)



(b)

Figure 4.3: Sensitivity and divergence of Lorentz current as a function of resolution. (a) Real components, (b) Imaginary components ($\alpha = 1$, $a = 8.635$ Np/m and $R_2 = 5$ cm).

$$J_m(z) = \frac{z^m}{2^m m!} \quad (4.14)$$

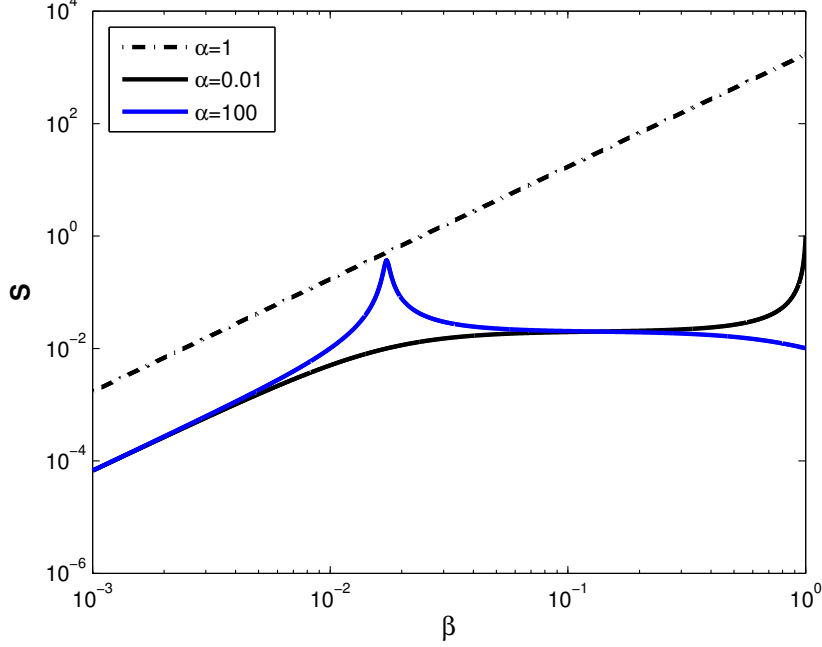


Figure 4.4: The sensitivity versus resolution plot for different conductivity contrast values. For sufficiently small resolution (β) values, sensitivity is higher when conductivity contrast approaches unity ($a = 8.635$ Np/m and $R_2 = 5$ cm).

With this simplifications, the slope of $S - \beta$ curve for small β is obtained as:

$$\frac{d \ln S_m}{d \ln \beta} = \frac{2m [\beta^{-2m}(1 + \alpha)^2 - \beta^{2m}(1 - \alpha)^2(2\varepsilon_m - 1)]}{\beta^{2m}(1 - \alpha)^2(2\varepsilon_m - 1) + \beta^{-2m}(1 + \alpha)^2 + 2\varepsilon_m(\alpha^2 - 1)} \quad (4.15)$$

where $\varepsilon_m = \frac{(kR_2)^m}{m!J_m(kR_2)2^m}$.

In Fig. 4.4, the sensitivity versus resolution plots for different conductivity contrast values are presented. The slopes of this graphs are described by equation (4.15). For Bessel functions in (4.15), small argument approximation is used. Consequently for large β values, the distribution of Fig. 4.4 is not accurate. For these values the change in sensitivity is oscillatory. This behavior is demonstrated in Fig. 4.11 for $\alpha = 1$. For small β values on the other hand, the distribution converges to true values. The small argument approximation is utilized in order to obtain an expression for slope of the

$S - \beta$ curve. As demonstrated in Fig. 4.4, as resolution (β) decreases the slope of sensitivity curves approaches to $2m$ independent of α . For $m = 1$, the slope of $S - \beta$ curve for MAET is the same as the one for EIT. That is an improvement of factor K^2 in the sensitivity, enhances the resolution by a factor K . The sensitivity-resolution curves for $\alpha = N$ and $\alpha = 1/N$ (N is a constant) are different for resolutions close to unity. However, improving the resolution, sensitivity values in cases where $\alpha = N$ and $\alpha = 1/N$ converge to the same value. The highest MAET sensitivity is obtained for $\alpha = 1$.

4.2.2 Sensitivity-Conductivity Contrast

In the next step, we investigate the interrelation between sensitivity and conductivity contrast. This behaviour is demonstrated in Fig. 4.5. The slopes of sensitivity-conductivity contrast curves are given in (4.16) for different β values. It is observed that for small conductivity contrast and resolution close to one the sensitivity is the greatest.

$$\frac{d \ln S_m}{d \ln \alpha} = \frac{(\alpha^2 - 1)(\beta^{2m} - \beta^{-2m} - 2\nu_m \beta^m) - 2\nu_m \beta^{-m}(1 + \alpha^2) + 2\alpha(\beta^m - \beta^{2m})}{(2\nu_m \beta^m - \beta^{2m})(1 - \alpha)^2 + 2\nu_m \beta^{-m}(\alpha^2 - 1) + \beta^{-2m}(1 + \alpha)^2} \quad (4.16)$$

where $\nu_m = \frac{J_m(k\beta R_2)}{J_m(kR_2)}$.

For $\beta = 1$, the sensitivity of MAET is constant with the value of one. For values of β smaller than unity, the sensitivity is lower. The slope of sensitivity curve approaches m or $-m$ as conductivity contrast approaches to zero or infinity. That is for $m = 1$, an improvement of factor K in conductivity contrast forces a degradation in system's sensitivity by the same factor K . Asymmetrical behaviour of MAET is illustrated in Fig. 4.5 for the resolutions close to unity.

4.2.3 Sensitivity-Outer Radius

Fig. 4.6 demonstrates pair-wise relation between sensitivity and outer radius R_2 . As outer radius increases, the sensitivity to the changes in conductivity contrast also

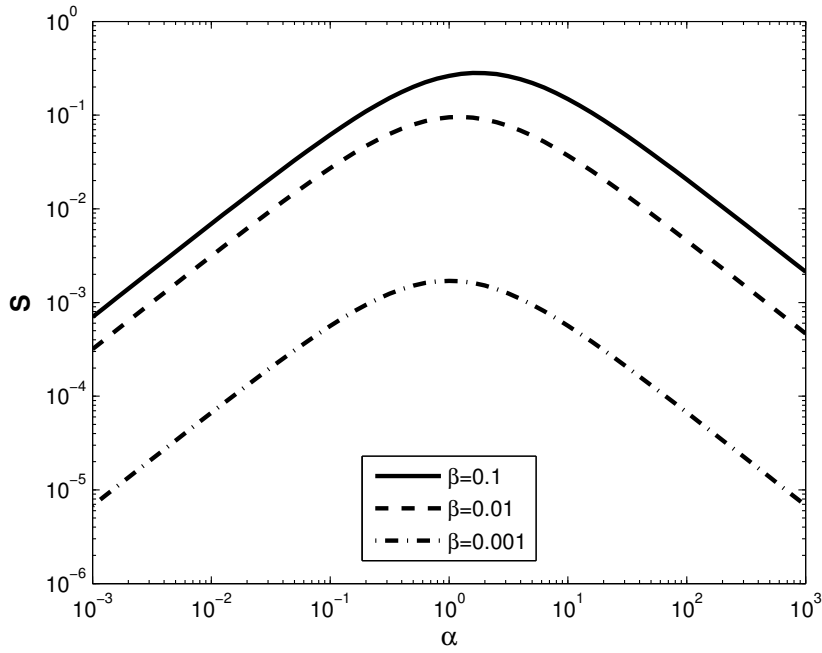


Figure 4.5: The logarithmic sensitivity versus conductivity contrast plot for different resolution values ($a = 8.635$ Np/m and $R_2 = 5$ cm).

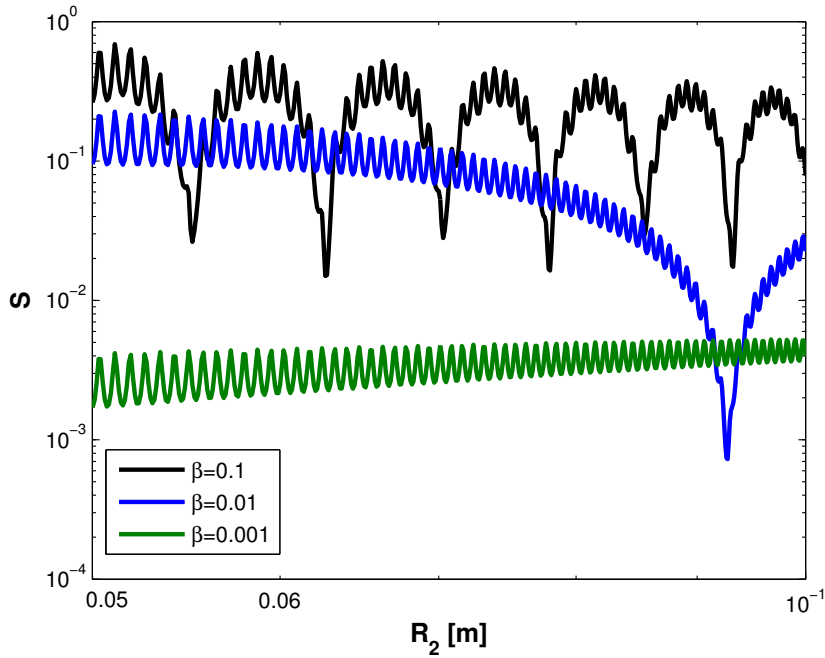


Figure 4.6: The logarithmic, sensitivity versus outer radius plot is given for different resolution values ($\alpha = 1$, $a = 8.635$ Np/m and $R_2 = 5$ cm).

increases for $\beta = 0.001$. For larger β values, the sensitivity is affected by the pressure distribution in the domain as the outer radius varies.

4.2.4 Sensitivity-Acoustic Attenuation

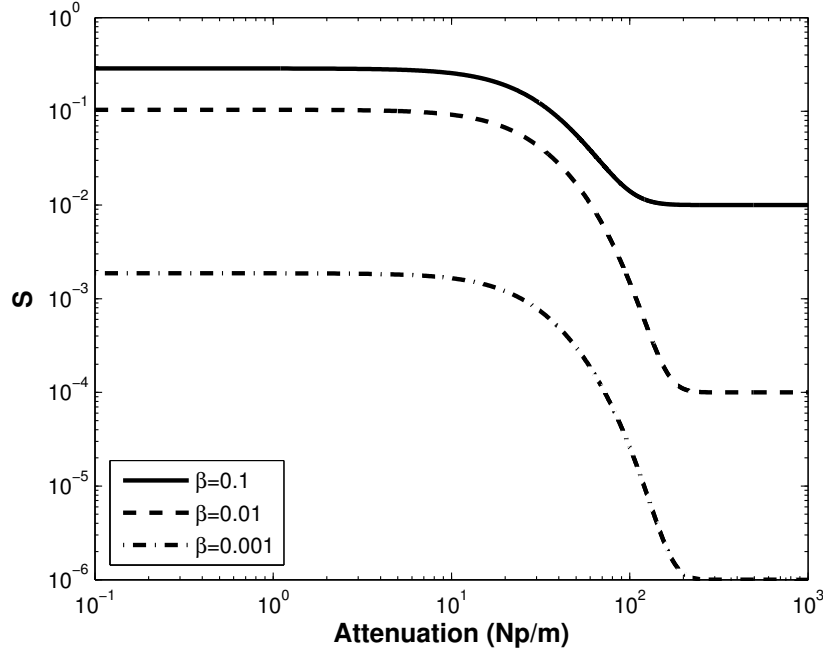


Figure 4.7: The logarithmic sensitivity versus acoustic attenuation plot for different resolution values ($\alpha = 1$ and $R_2 = 5$ cm).

The relation between acoustic attenuation and sensitivity is given in Fig. 4.7. As acoustic attenuation increases, the sensitivity of the MAET decreases. For acoustic attenuation values greater than 100 Np/m, the sensitivity of MAET imaging system becomes independent of the attenuation. In this calculations, conductivity contrast is $\alpha = 1$. For attenuation values under 10 Np/m the sensitivity does not vary much.

4.2.5 Sensitivity-Frequency

In order to investigate the behavior of MAET with respect to frequency, the sensitivity of imaging system is obtained for different frequency values. It is important to identify the parameters of the imaging system that are frequency dependent. The permittivity, electrical conductivity and acoustic attenuation of the medium are all

frequency dependent. The frequency dependency of acoustic attenuation, $a(f)$, can be represented as:

$$a(f) = a f^\eta \quad (4.17)$$

For the breast fat tissue, attenuation at 1 MHz is $a = 4.3578$ Np/m and material parameter η is 1.0861 [24]. The other frequency dependent electrical parameters can be obtained from 4 element Cole-Cole dispersion model as follows [25]:

$$\varepsilon'(f) = \varepsilon_\infty + \sum_{n=1}^4 \frac{\Delta\varepsilon_n}{1 + (j2\pi f\tau_n)^{1-\alpha_n}} + \frac{\sigma_{DC}}{j2\pi f\varepsilon_0} \quad (4.18)$$

The complex permittivity of the tissues can be extracted from (4.18). Where ε_∞ is the permittivity at frequencies where $\omega\tau \gg 1$ and ε_s is the permittivity at frequencies where $\omega\tau \ll 1$. The magnitude of dispersion, $\Delta\varepsilon_n$, is $\varepsilon_s - \varepsilon_\infty$. τ_n is the n^{th} polarization constant and α_n is the n^{th} distribution parameter. These parameters describe the complex permittivity of tissues at different frequency ranges. For the tumor and breast fat tissue, the parameters of (4.18) are given in Table 4.1.

Table 4.1: Dispersion parameters for fat and blood tissue [24].

	Breast fat	Tumor (Blood)
ε_∞	2.5	4
$\Delta\varepsilon_n$	3, 15, 5×10^4 , 2×10^7	56, 5200, 0, 0
τ_n	17.68 ps, 63.66 ns, 454.7 μ s, 13.26 ms	8.377 ps, 132.629 ns, 159.155 μ s, 15.915 ms
α_n	0.1, 0.1, 0.1, 0	0.1, 0.1, 0.2, 0
σ_{DC}	0.01	0.7

It is observed that similar to previous cases, as the resolution (β) decreases, so does its sensitivity to changes in conductivity contrast. In Fig. 4.8, the acoustic attenuation causes the sensitivity to drop at higher frequencies. For $\beta = 10^{-3}$ the sensitivity maximum at 3.56 MHz.

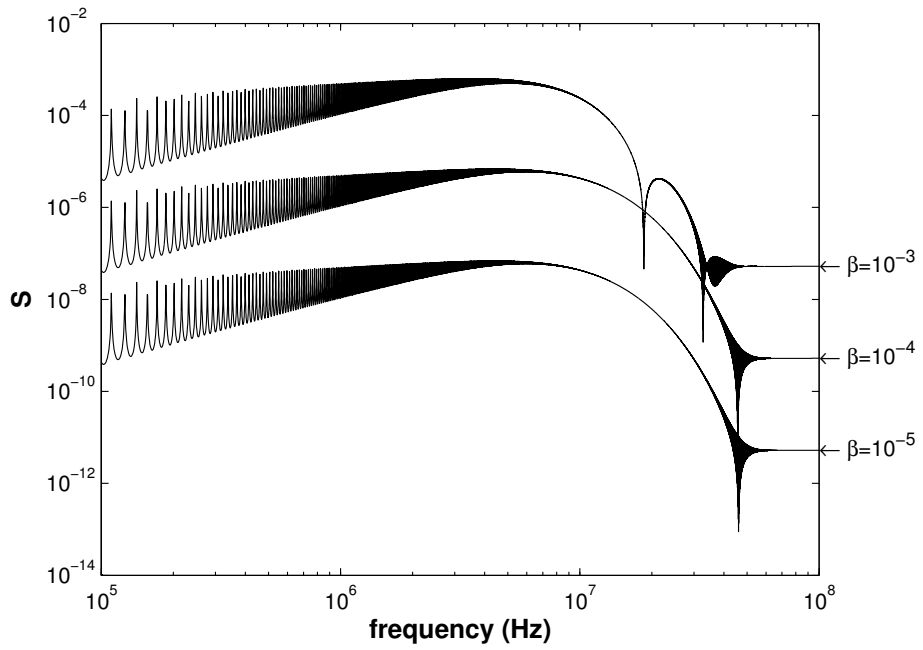


Figure 4.8: The logarithmic sensitivity versus frequency plot for different resolution values ($\alpha = 1$ and $R_2 = 5$ cm).

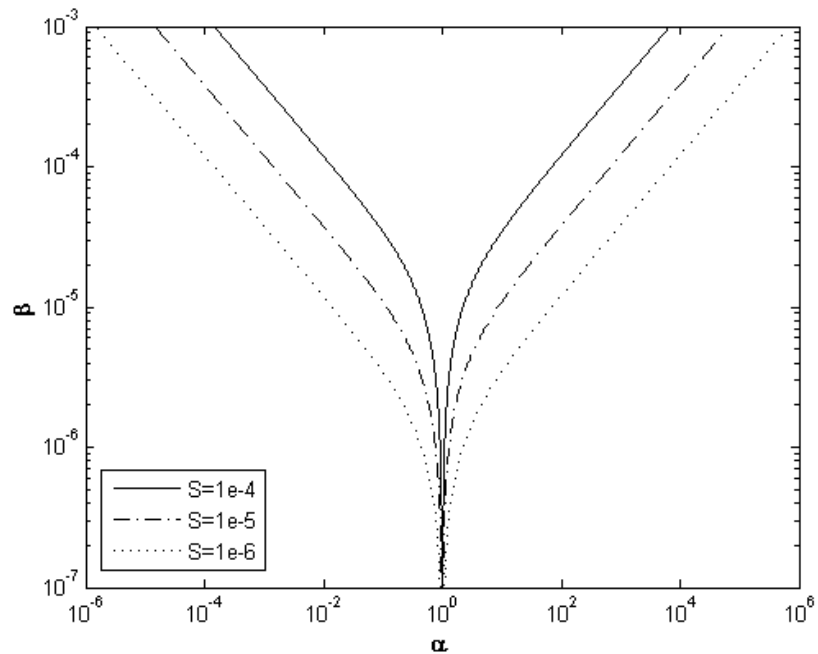


Figure 4.9: The logarithmic, resolution versus conductivity contrast plot for different sensitivity values.

4.2.6 Resolution-Conductivity Contrast

In Fig. 4.9, the relation between resolution and conductivity contrast is given. For small β where approximation for Bessel function is valid, the slope of $\beta - \alpha$ curve is $1/2m$. As $\beta \rightarrow 0$ the slope of the curve goes to infinity. The resolution curve's behaviour is oscillatory for β close to unity.

4.2.7 Summary of Pair-wise Relations

Similar to [6], we define noise as $d\phi/\phi$ and $d\alpha/\alpha$ as accuracy of the imaging system. The fractional change in electric potential is equated to noise to obtain the best resolution and conductivity contrast values. Therefore, pair-wise relations for sensitivity, resolution, conductivity contrast, accuracy, noise, acoustic attenuation and frequency are defined as ($m = 1$):

- Improving noise by a factor K , improves accuracy by the same factor K .
- An improvement in resolution by a factor of K , degrades the sensitivity by factor K^2 .
- An improvement by a factor K in conductivity contrast reduces the sensitivity of the MAET by the same factor, K .
- An improvement by a factor K^2 in conductivity contrast, degrades the resolution of the MAET by a factor K .
- Increasing acoustic attenuation degrades sensitivity.
- For $\beta = 0.001$, $\alpha = 1$ and $R_2 = 5$ cm, maximum sensitivity is obtained at 3.56 MHz.

4.3 Conformal Mapping (Eccentric Inhomogeneities)

In order to assess the performance of the MAET for inhomogeneities anywhere inside an object, conformal mapping is used to map eccentric circular geometries to concentric ones (Fig. 4.10). The expression for transforming a circular inhomogeneity of

radius ρ and location (α_c, φ) inside a circle of radius R_2 in z -domain to concentric circles with radii of R_1 and R_2 in w -domain is [16]:

$$w = \frac{ze^{-i\varphi} - cR_2}{cze^{-i\varphi} - R_2} R_2 \quad (4.19)$$

where c is the solution of the following equation given that $|c| < 1$:

$$\alpha_c R_2 c^2 - (\alpha_c^2 + R_2^2 - \rho^2)c + \alpha_c R_2 = 0 \quad (4.20)$$

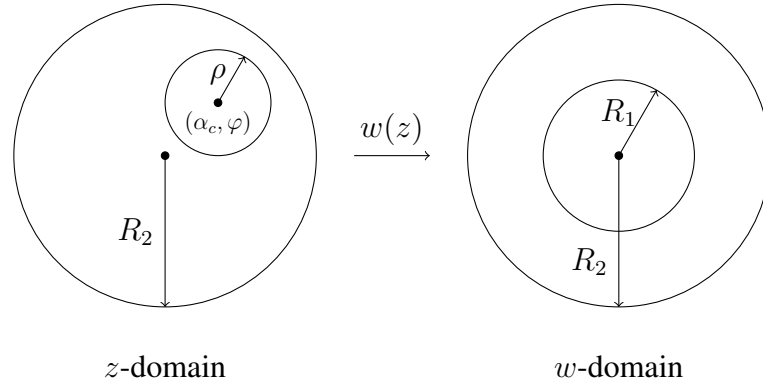


Figure 4.10: Conformal mapping from z -domain to w -domain, defined by function $w(z)$ in (4.19).

The relation between R_1 , R_2 , α_c and ρ is:

$$R_1 = \left| \frac{\alpha_c - \rho - cR_2}{c(\alpha_c - \rho) - R_2} \right| R_2 \quad (4.21)$$

Given equation (4.21), we obtained an expression relating the radii of inner circles in z and w -domain for small inhomogeneities ($\rho \rightarrow 0$):

$$\lim_{\rho \rightarrow 0} \frac{R_1}{\rho} = \frac{R_2^2}{R_2^2 - \alpha_c^2} \quad (4.22)$$

Consequently for small ρ 's, the closer the inhomogeneity is to the boundary of the object, the greater is the imaging system's resolution. The parameters effecting the radius of inner circle (R_1) are the offset of the inhomogeneity from origin (α_c) and radius of outer circle (R_2). This information complements the equation (4.13). For example let $R_2 = 1$, then an inhomogeneity of radius $\rho = 0.075$ and an offset $\alpha_c = 0.5$ corresponds to a circle of radius $R_1 = 0.1$ in concentric case. The improvement

in the resolution is 33 %. From the summary of section 4.2.7, the improvement in the resolution can be related to the improvement in conductivity contrast or sensitivity of the system. This corresponds to an improvement in the conductivity contrast or the sensitivity by 79 %.

4.4 Comparison to EIT Sensitivity

For EIT, Seagar et al. [6] derived the sensitivity expression as:

$$S_{EIT} = \frac{-4\alpha\beta^{2m}}{(1 + \alpha)^2 - (1 - \alpha)^2\beta^{2m}} \quad (4.23)$$

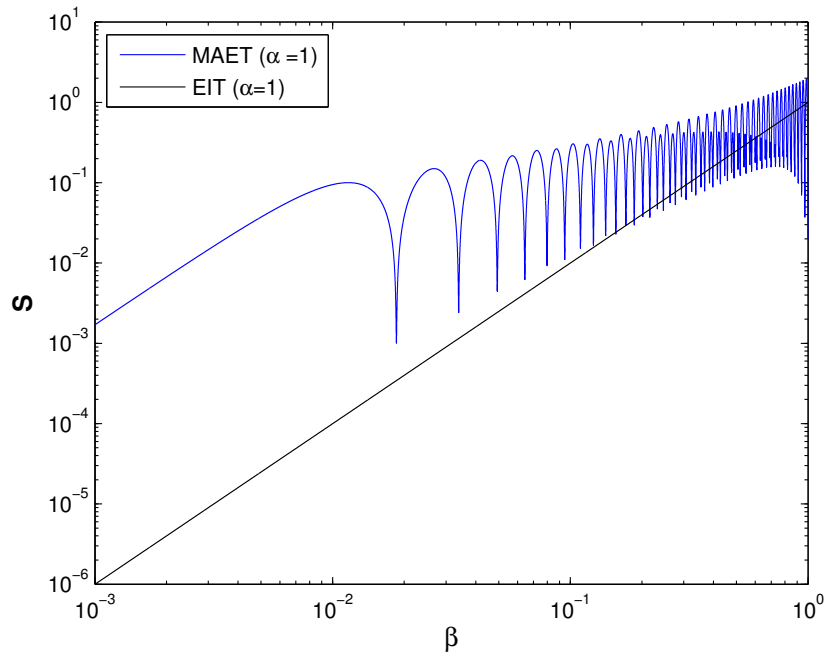
In Fig. 4.11, the sensitivity expression of EIT (4.23) is compared to the sensitivity expression of MAET (4.13). If $m = 1$ for the resolutions smaller than 0.6, MAET has greater sensitivity. For $m = 2$ on the other hand, MAET becomes more sensitive if the resolution is smaller than 0.2. The slope of $S - \beta$ curves are $2m$ for small resolutions in both EIT and MAET.

4.5 Arbitrary Periodic Boundary Excitations

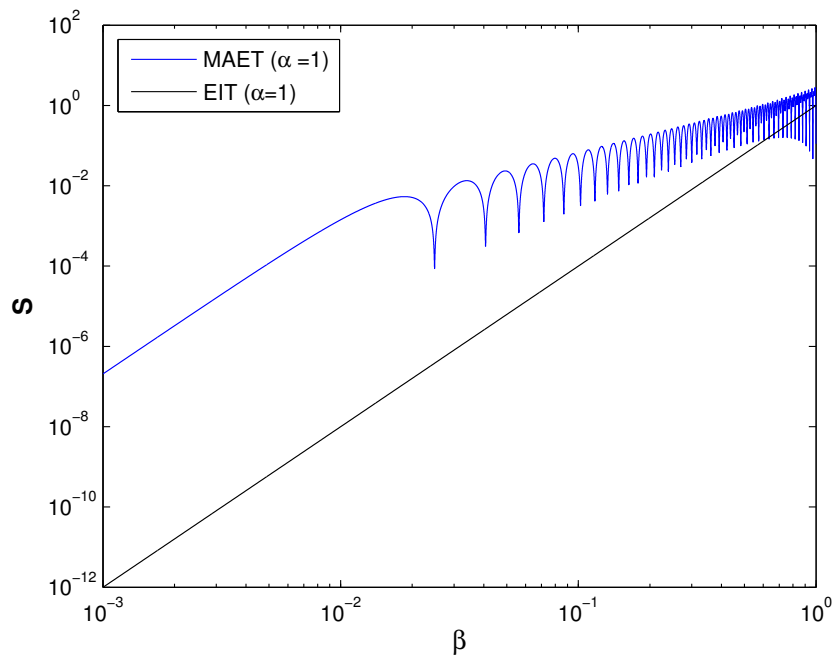
The sensitivity expression for harmonic cases can be combined to represent other periodic excitations. Given equation (4.8), the sensitivity distribution for an arbitrary excitation consisting of m terms is as follows:

$$S(\theta) = \frac{V_1S_1 + V_2S_2 + \dots + V_mS_m}{V_1 + V_2 + \dots + V_m} \quad (4.24)$$

where $V_m = z_{mm}(\gamma_m e^{jm\theta} - \delta_m e^{-jm\theta})$. For example given the acoustic excitation of Fig. 4.12, the sensitivity at angles $\theta = 0$ and $\theta = \pi/3$ are presented in 4.13. The sensitivity for the arbitrary periodic case is compared to the harmonic case. It is observed that the fractional change in the electric potential at $\theta = 0$ is greater than the change at $\theta = \pi/3$. For the locations where the electric potential is zero, the sensitivity is not defined.



(a) $m = 1$



(b) $m = 2$

Figure 4.11: The sensitivity of MAET and EIT as a function of resolution for (a) $m = 1$ and (b) $m = 2$. The conductivity contrast is unity in both cases.

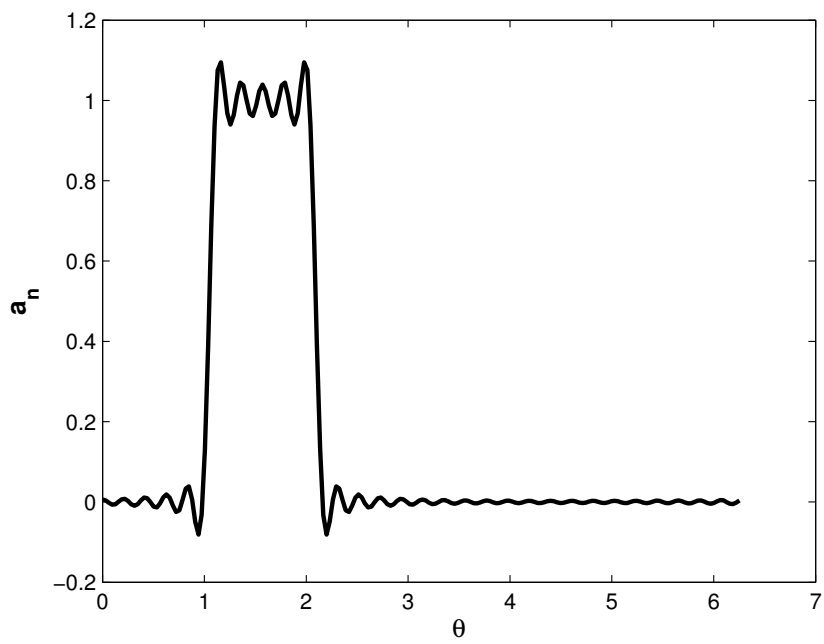
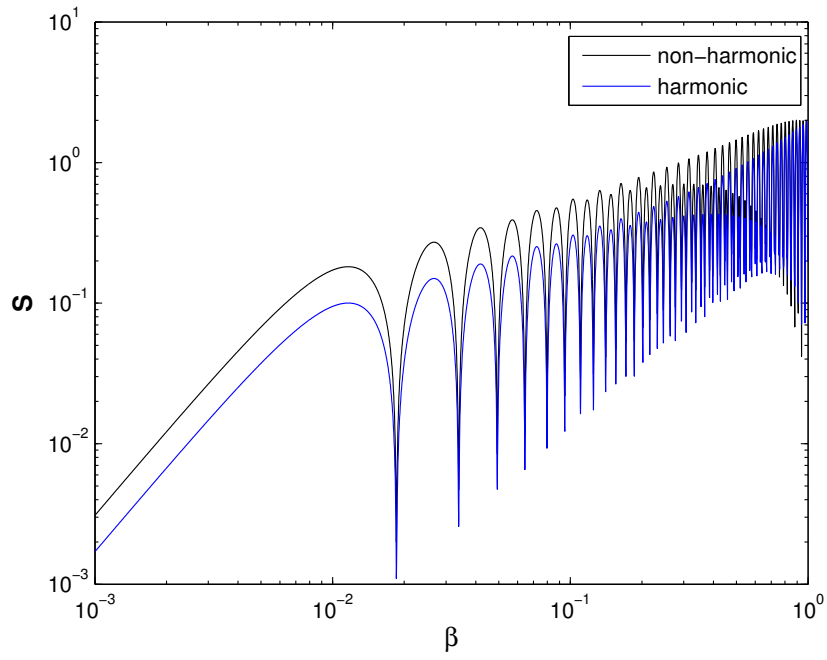
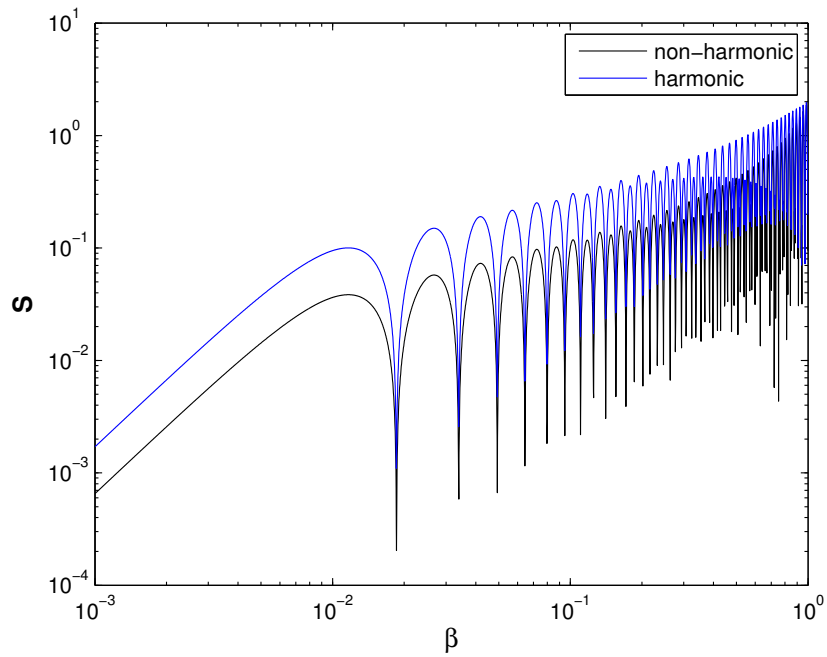


Figure 4.12: The square pulse centered at $\theta = \pi/2$ and angular length of $\pi/3$.



(a) $\theta = 0$



(b) $\theta = \pi/3$

Figure 4.13: The sensitivity distribution of harmonic and non-harmonic excitations at $\theta = 0$ and $\theta = \pi/3$.

CHAPTER 5

HEAT ANALYSIS FOR MAET

In this chapter we investigate the tissue heating in MAET for a simplified 2D breast model (Fig. 5.1). Due to acoustic excitation and induced Lorentz currents, heat sources emerge inside the body. Acoustic absorption and resistive heating are the mechanisms responsible for these sources. The aim of this study is to determine the extent of tissue heating and whether it may cause any damage to the tissues or not.

First the steady state acoustic pressure distribution is evaluated for the breast model of Fig. 5.1. The resultant acoustic velocity distribution generates Lorentz currents in the presence of a static magnetic field. Next in the AC/DC module of the COMSOL, we solve the differential equation for the electric potential, from which induced current, displacement current and Lorentz currents are derived. The aforementioned currents and the acoustic intensity are the heat sources. But before calculating the temporal temperature in the model, first we solve for the steady state temperature distribution where metabolic heat generation, blood perfusion and heat loss to ambient air are the only source of heat exchange. Finally the steady state solution is set as the initial condition to evaluate the temperature increase due to the acoustic and electric sources. These steps are thoroughly explained in the following sections.

5.1 Acoustic Problem

The simulation for the acoustic problem is performed on the modified breast model. The breast model of Fig. 5.1 is updated to include a 16 element linear phased array transducer (Fig. 5.2). The acoustic properties of tissues in the simplified breast model

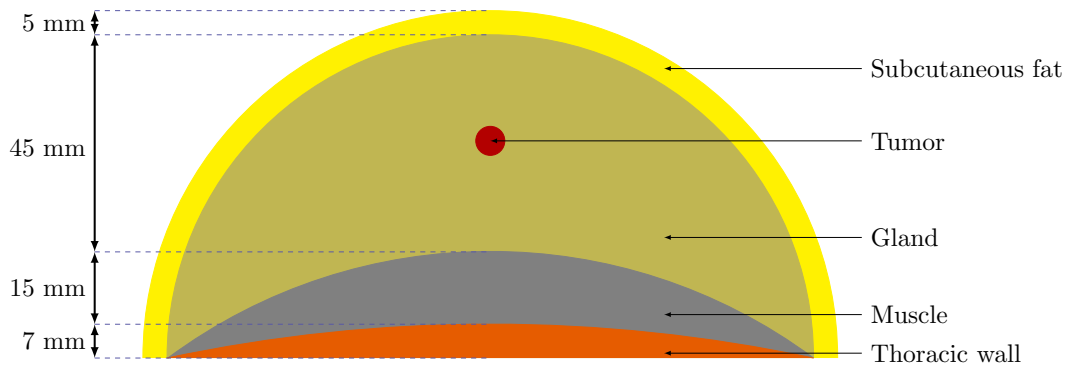


Figure 5.1: A simplified 2D breast model composed of subcutaneous fat, gland, tumor, muscle and thoracic muscle tissues [26].

are given in Table 5.1.

Table 5.1: The acoustic properties of breast tissue at 1 MHz [27].

Tissues	Density (kg/m ³)	Speed of sound (m/s)	Attenuation (Np/m)
Subcutaneous fat	980	1520	4.3578
Gland	1041	1505	8.635
Muscle	1090	1588	7.1088
Tumor (blood)	1041	1564	2.3676

The length of each elements of LPA transducer is 0.65 mm and the separation between elements is 0.35 mm. On each of the elements an inward boundary acceleration is defined. The value for this acceleration is 3.841×10^6 m/s². The resultant pressure distributions peak value is 1.7 MPa which is the safety limit for acoustic pressure at 1 MHz [28]. The breast model of Fig. 5.2 is meshed with triangular elements. The maximum length of elements is 0.3 mm which is approximately equal to one fifth of acoustic wavelength. The Helmholtz equation is solved for the acoustic pressure in COMSOL [29]:

$$\nabla \cdot \left(\frac{1}{\rho} \nabla p \right) + \frac{k^2}{\rho} p = 0 \quad (5.1)$$

$$\mathbf{n} \cdot \frac{1}{\rho} \nabla p = p \frac{j\omega}{Z_i}$$

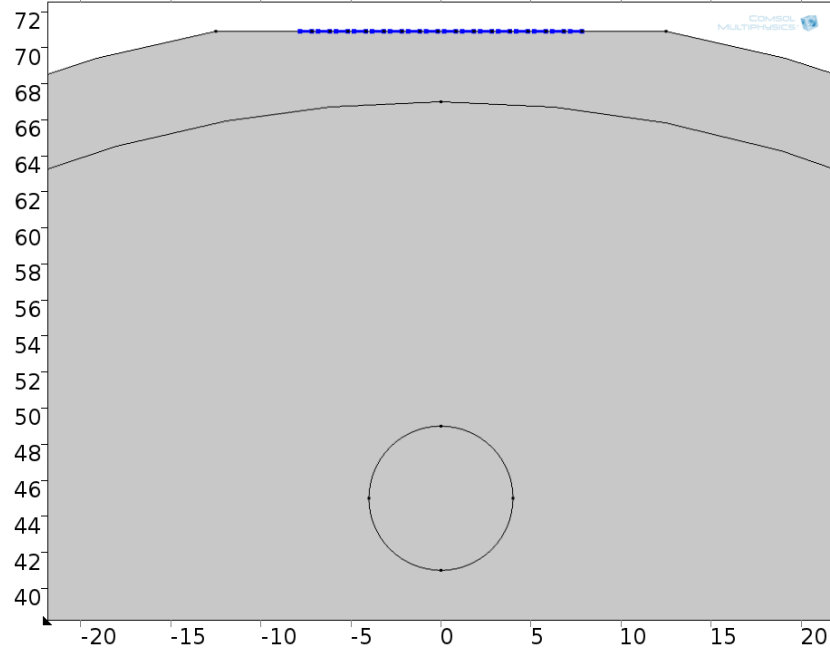


Figure 5.2: The modified breast model with the introduction of 16 element LPA transducer. The LPA elements (blue lines) are modeled as normal boundary acceleration.

Here p (Pa) is acoustic pressure, ρ is density, $k = \frac{\omega}{c} - ja$ is wave number, a is acoustic attenuation, ω is angular velocity and c is speed of sound. $Z_i = 1.2 \text{ (kg/m}^3\text{)} \times 343 \text{ (m/s)}$ is the acoustic impedance of the domain outside our model which is air in this case. \mathbf{n} is the unit normal vector. The resultant pressure distribution is demonstrated in Fig. 5.3. The maximum value of acoustic intensity is right below the transducer.

5.2 Electrical Problem

The differential equation for the electrical problem of MAET is given in chapter 2. Equation (2.13) is modified to include the displacement currents as well. In COMSOL, following differential equation and boundary condition are solved for electric potential:

$$\nabla \cdot (-(\sigma + j\omega_e \epsilon_0 \epsilon_r) \nabla \phi + \sigma \mathbf{v} \times \mathbf{B}_0) = 0, \text{ in } \Omega \quad (5.2)$$

$$\mathbf{n} \cdot (-(\sigma + j\omega_e \epsilon_0 \epsilon_r) \nabla \phi + \sigma \mathbf{v} \times \mathbf{B}_0) = 0, \text{ on } \partial\Omega$$

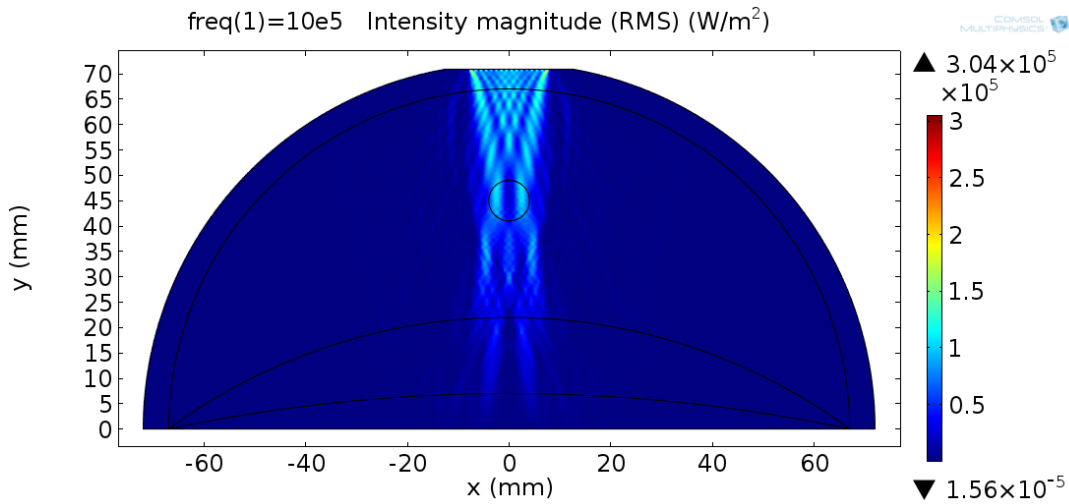


Figure 5.3: The steady state magnitude of acoustic pressure intensity in the simplified 2D breast model.

Here ϕ (V) is the electric potential, v (m/s) is acoustic velocity, B_0 (T) is the magnetic field, σ (S/m) is electrical conductivity, ω_e (rad/s) is electrical angular frequency, ϵ_0 is relative permittivity of free space and ϵ_r is relative permittivity of tissues.

The electrical properties of tissues in simplified breast model are given in Table 5.2.

Table 5.2: The electrical properties of breast tissues at 1 MHz [30–32].

Tissue	Relative permittivity (1)	Electrical conductivity (S/m)
Subcutaneous fat	23.7	0.0257
Gland	1430	0.603
Muscle	1840	0.503
Tumor (blood)	3030	0.8221

The obtained electric current density is demonstrated in Fig. 5.4. This current density is composed of Lorentz and conductive currents. Since the electrical conductivity of the fat tissue is low, the current density is lower in this region compared to others. Also with the conductivity of 0.8221 S/m, the blood tissue is the most conductive and the current density is higher in this region.

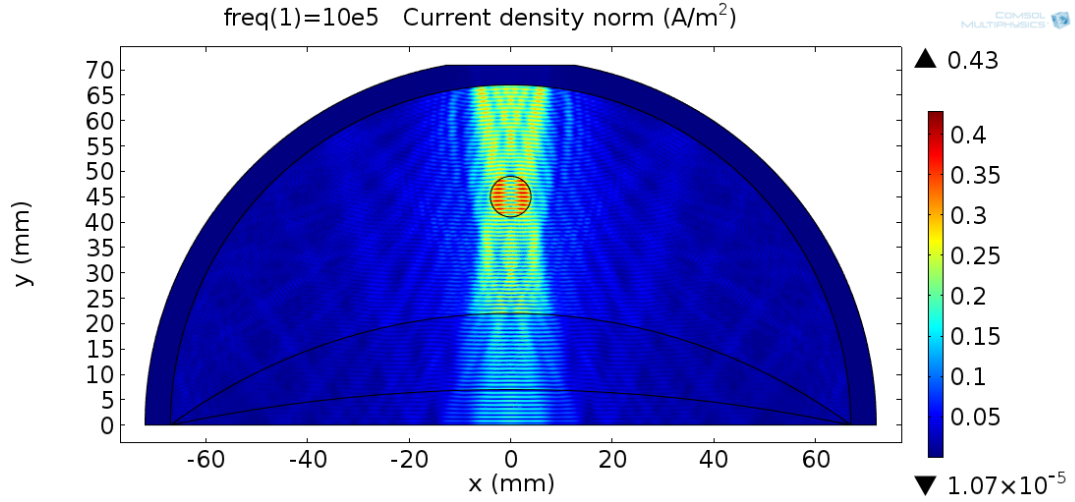


Figure 5.4: The total current density distribution in the simplified 2D breast model.

5.3 Heat Problem

In the electric problem, we have calculated the total current density distribution. Due to resistive power dissipation, the temperature in the tissues increases. There are also heating related to acoustic absorption in the tissues. The heat problem of MAET is modeled by Penne's Bioheat equation [33]:

$$\rho C_p \frac{\partial T}{\partial t} = \nabla \cdot (k_T \nabla T) + Q_{bio} + Q - \rho_b C_b \omega_b (T - T_b) \quad (5.3)$$

Here T (K) is temperature, C_p (J/kg·K) is specific heat capacity, k_T (W/m·K) is thermal conductivity, Q_{bio} (W/m³) is metabolic sources, Q (W/m³) is external heat sources (acoustic and electrical) and ω_b (1/s) is the blood perfusion rate of tissues.

The homeostatic temperature of human body is 37 °C. To replicate this behavior, the exterior boundary condition of muscle tissue is set to 37 °C. To model the radiation heat loss between the tissue and the exterior air of 20 °C, surface to ambient radiation condition is selected [29, 34]:

$$\mathbf{n} \cdot (k_T \nabla T) = \epsilon \sigma_{S-B} (T_{ambient}^4 - T^4) \quad (5.4)$$

Where ϵ (1) is emissivity of the human body and σ_{S-B} (W/m²·K⁴) is Stefan-Boltzmann

constant. The heat loss due to convection and evaporation at the exterior boundary is represented by the following heat loss factor:

$$\mathbf{n} \cdot (k_T \nabla T) = h(T_{ambient} - T) \tag{5.5}$$

Here $h = 7.01 \text{ W/m}^2 \cdot \text{K}$ is the total heat transfer coefficient. The tissue properties in heat problem are given in Table 5.3.

Table 5.3: Breast tissues and tumor’s thermal properties [35].

Tissues	Specific heat (J/kg·K)	Thermal conductivity (W/m·K)	Metabolic heat (W/m ³)	Blood perfusion (W/m ³ ·K)
Subcutaneous fat	2348	0.21	400	800
Gland	2960	0.33	700	2400
Muscle	3421	0.49	700	2400
Tumor (blood)	3617	0.52	42000	48000

In this model, we first calculate the steady state heat distribution in the body in absence of external sources, i.e. acoustic and electric sources. This distribution is demonstrated in Fig. 5.5. In this simulation, the radius of tumor is 4 mm and its depth is 27 mm.

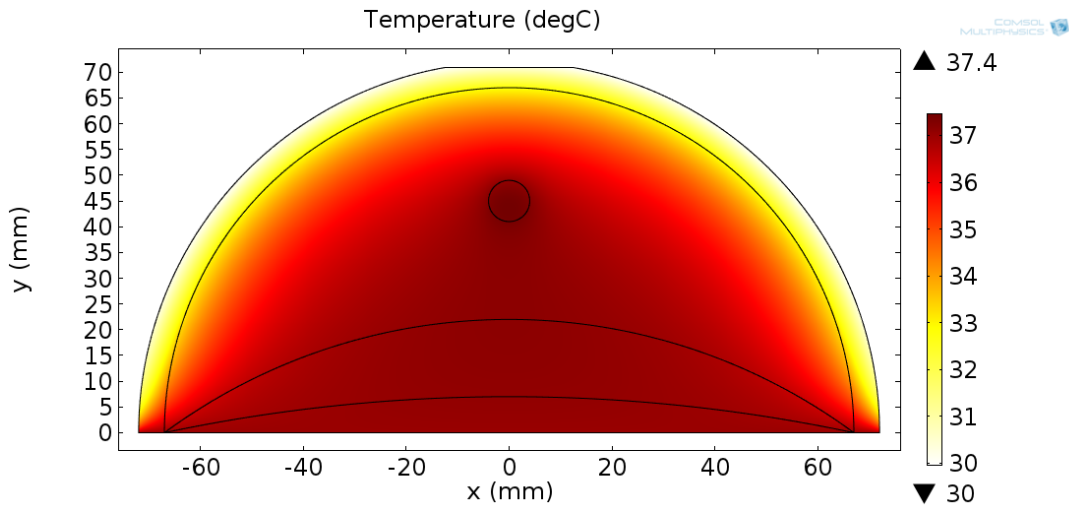


Figure 5.5: The steady state heat distribution in absence of electrical and acoustic heat sources.

In Fig. 5.5 the hottest tissue in the breast is tumor due to its high metabolic heat generation (37.45 °C). Because of surface radiation to a 20 °C ambient air, the tem-

perature in extremities of body is lower. The temperature drops to 29.96 °C in these regions.

The temperature distribution of Fig. 5.5 is set as the initial condition in the transient heating problem of the breast tissue. The added source to Penne's equation are electrical and acoustic. The heat source due to acoustic wave absorption is given as [33]:

$$Q_{acoustic} = 2aI \quad (5.6)$$

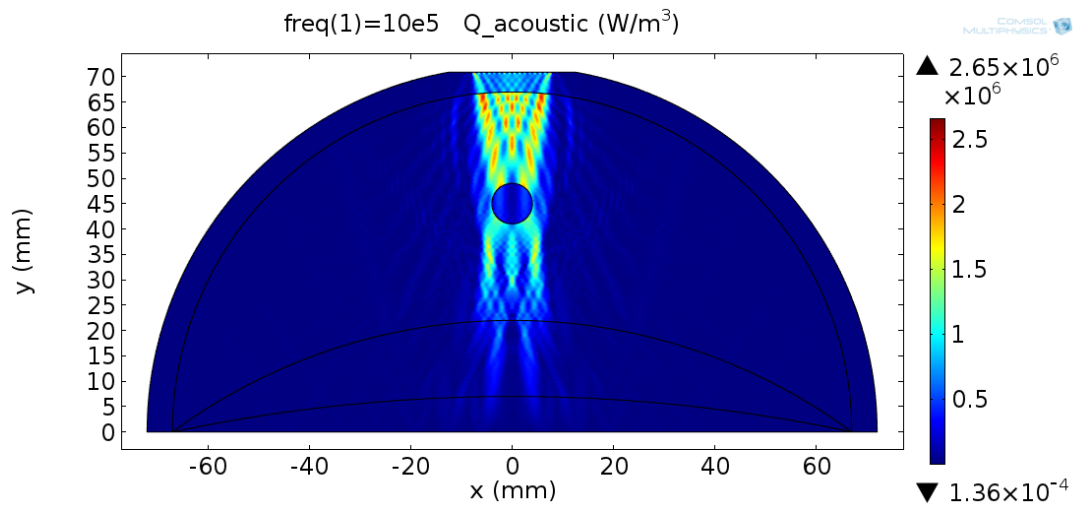
Here I (W/m²) is the magnitude of acoustic intensity. The source of electrical heating is the current density of Fig. 5.4, which is given as:

$$Q_{electrical} = \frac{1}{\sigma} |\mathbf{J}|^2 \quad (5.7)$$

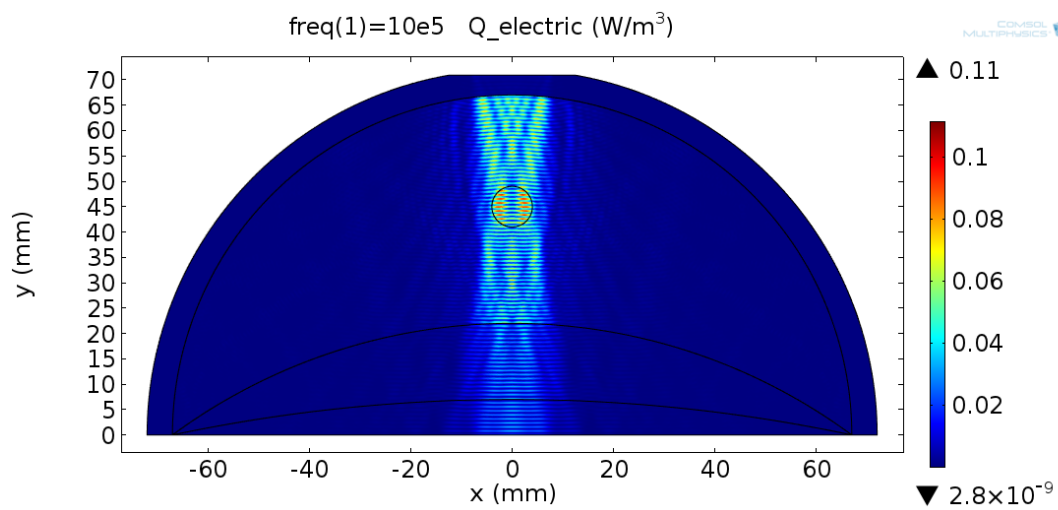
The distribution of these sources are given in Fig. 5.6. The acoustic heat generation in the model is several orders of magnitude greater than the heat generation due to resistive current dissipation. In Fig. 5.6(a), the highest heat generation is in the gland tissue ($a = 8.635$ Np/m).

The transient heat problem is solved with the Backward Differentiation Formula (BDF) of 5th order. The relative tolerance is 0.01 and maximum time step is 0.01 s [33]. A sinusoidal boundary acceleration of 3.841×10^6 m/s² and frequency of 1 MHz is applied to the medium for a second. The resultant heat distribution is demonstrated in Fig. 5.7(a). After terminating the acoustic wave, the heat redistributes inside the body. The temperature distribution at 10 seconds is also given in Fig. 5.7(b). The maximum temperature in Fig. 5.7(a) is 37.67 °C. The acoustic pressure is the main cause of this temperature increase. After a second the sources are cut off and tissues temperature decreases with time. It takes minutes for the tissue to obtain its steady state distribution. In Fig. 5.8, the spatial temperature rise relative to the initial condition (Fig. 5.5) is presented at $t = 1$ s. The maximum value of temperature is 0.62 °C in the gland tissue.

Thermal safety considerations of MAET imaging technique is investigated for the

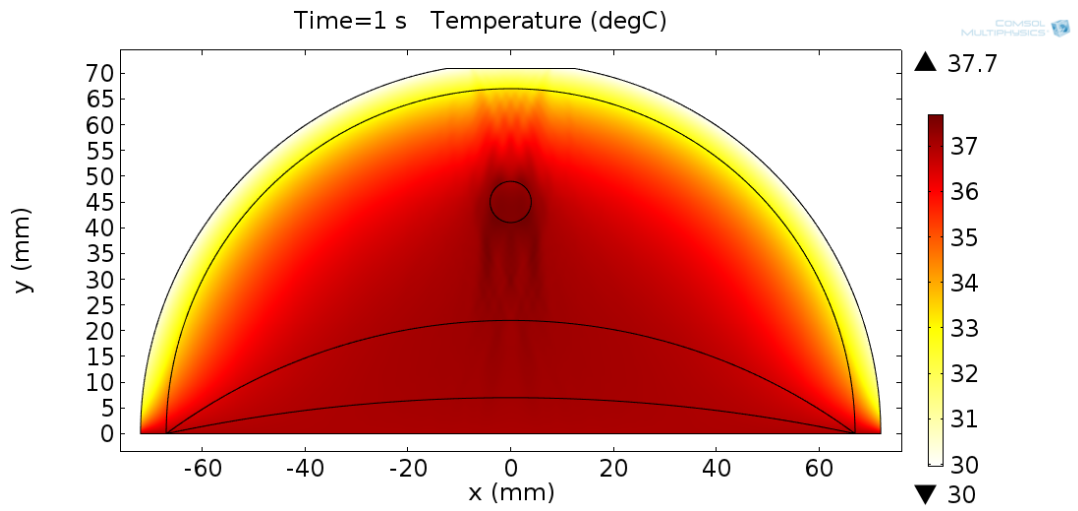


(a)

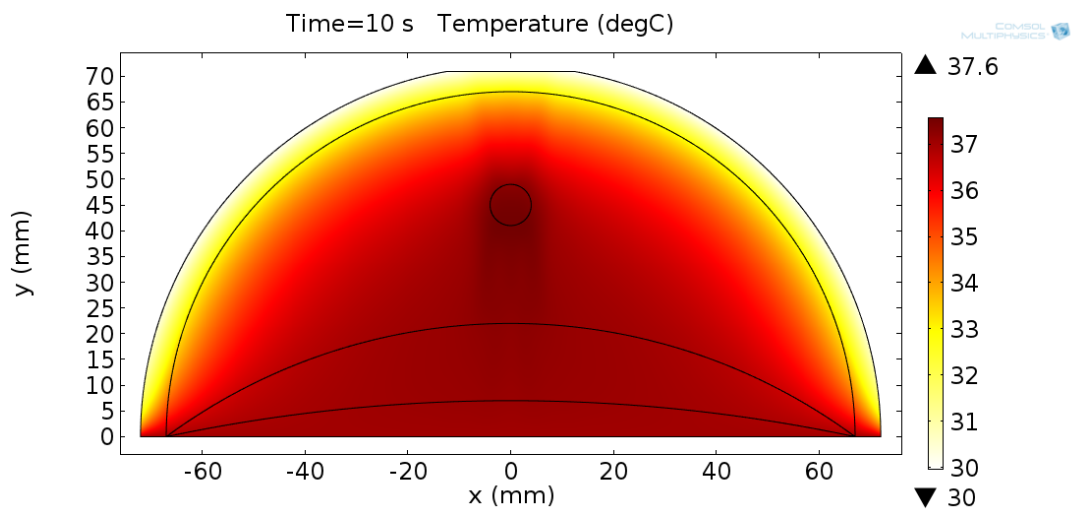


(b)

Figure 5.6: (a) The distribution of acoustic heat source and (b) electric heat source in the simplified 2D breast model.



(a) 1 second



(b) 10 seconds

Figure 5.7: The heat distribution at (a) $t = 1$ s and (b) $t = 10$ s, where the tissue is acoustically excited for a second.

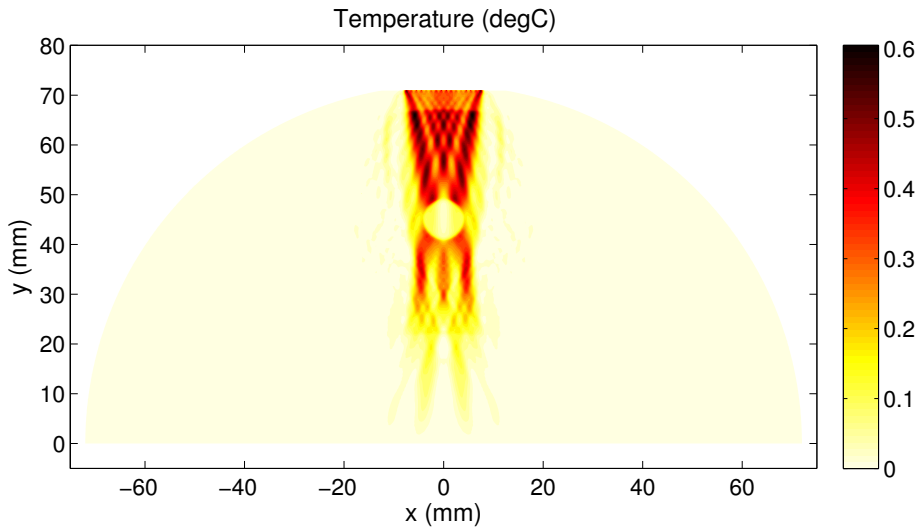


Figure 5.8: The temperature increase in the simplified 2D breast model at $t = 1$ s relative to its initial value.

simplified 2D breast model. The steady state heat distribution in the model is simulated in absence of acoustic excitation. Then the acoustic pressure is applied for 1 second and resultant temperature distribution is presented. The absorption of acoustic waves in the tissues is the main heat source in Pennes' Bioheat equation. There are also heat sources due to resistive dissipation of total current density in the medium. It is concluded that the maximum temperature increase in the tissues from these heat sources is within the safety limits of medical applications.

CHAPTER 6

CONCLUSION

6.1 Summary

An analytical solution for the forward problem of MAET is obtained for 2D concentric bodies. Based on this solution a sensitivity expression is derived. It is the ratio of the fractional change in electric potential to the fractional change in the conductivity contrast. The sensitivity of MAET depends on resolution, conductivity contrast, acoustic wave number and the dimensions of the body. By implementing conformal mapping, the sensitivity expression is modified for eccentric bodies. The sensitivity expression for different harmonics are combined to obtain a sensitivity expression for non-harmonic acoustic boundary accelerations distributions.

For a simplified 2D breast model, the steady state heat distribution is calculated numerically. Then an acoustic excitation is applied to the body and the resultant temperature change is observed. It is concluded that the temperature increase in MAET imaging is within thermal safety limits (given that the pressure is within the safety limits).

6.2 Discussion

The analytical solutions obtained for the acoustic and electrical problems of MAET are compared to the numerical solutions of COMSOL Multiphysics. For each node of the mesh, the relative error between analytical and numerical solutions were obtained. The average error in absolute value for acoustic pressure is 0.064 %. For

the electrical potential this value is 0.14 %. The overall error in both solutions are acceptable. It is observed that the largest errors between the analytical and numerical solutions are the points where electric potential or acoustic pressure is zero. In these points both solutions are practically zero, however analytical solution is orders of magnitude less than the numerical solution.

A sensitivity expression for MAET is derived in this thesis and its characteristic behaviors were examined. The expression depends on resolution, conductivity contrast, acoustic wave number and the dimensions of the object of interest. For the tissue properties of the gland tissue the pair-wise relation between sensitivity and other parameters are given. It is observed that a degradation of factor K in the sensitivity or conductivity contrast of the MAET, introduces an improvement of \sqrt{K} in the resolution. Also to improve the conductivity contrast of MAET by a factor K , sensitivity must be degraded K times. It is observed that as the acoustic attenuation of a body increases, the sensitivity degrades independent of the resolution. The frequency of acoustic pressure does also effect the sensitivity. As frequency increases, so does the acoustic attenuation. Consequently the sensitivity is lower for high frequency excitations. The frequency of operation also changes the steady state acoustic pressure distribution and the conductivity contrast of the object. For the first and second harmonic boundary excitation, it is demonstrated that the overall sensitivity of MAET is greater than EIT. For higher frequency harmonics, the improvements in the sensitivity of MAET are more dominant when they are compared to the sensitivity of EIT. Although the sensitivity expression is derived for harmonic acoustic boundary excitations, for arbitrary boundary excitations, the harmonic components of the periodic signal are obtained and a sensitivity expression is defined for such an arbitrary excitation.

For an imaging method to be feasible, it must not cause any harm to living tissues. In MAET, ultrasound transducers excite the body. The amplitude of pressure distribution inside the body must be in safety limits. At an operation frequency of 1 MHz, this value is 1.7 MPa. The other concern is the tissue heating due to absorption of acoustic waves and power dissipation due electrical currents. In a simplified breast model, given a maximum pressure of 1.7 MPa, we have presented the heating characteristics. For a case where the model is excited for 1 second, the maximum temperature

increase is below the safety limit (1 °C).

6.3 Future Work

Here the sensitivity expression for MAET is derived for electric potential measurements. The Lorentz current distribution inside a body can also be sensed by coils (LFEIT). A sensitivity expression will be derived for the LFEIT imaging method.

For transient acoustic excitations, time dependent sensitivity expression will be calculated for MAET. Since the sensitivity expression is derived for the all harmonic excitations, given the harmonics of Lorentz current density in the boundary and the interfaces at a specific time, a sensitivity expression will be defined for that particular time.

3D analysis for the heat problem of MAET will be performed in COMSOL. Off plane heat transfer characteristic and 3D heat emission effects will be contributing to the overall temperature distribution in this model as well.

REFERENCES

- [1] D. C. Barber and B. H. Brown, “Applied potential tomography,” *Journal of Physics E: Scientific Instruments*, vol. 17, no. 9, p. 723, 1984.
- [2] K. Paulson, W. Lionheart, and M. Pidcock, “Optimal experiments in electrical impedance tomography,” *IEEE Transactions on Medical Imaging*, vol. 12, pp. 681–686, Dec 1993.
- [3] P. Metherall, D. C. Barber, R. H. Smallwood, and B. H. Brown, “Three-dimensional electrical impedance tomography,” *Nature*, vol. 380, pp. 509–512, Apr 1996.
- [4] N. G. Gençer, *Electrical impedance tomography using induced currents*. PhD thesis, Middle East Technical University, 1993.
- [5] N. G. Gencer, M. Kuzuoglu, and Y. Z. Ider, “Electrical impedance tomography using induced currents.,” *IEEE transactions on medical imaging*, vol. 13, no. 2, pp. 338–350, 1994.
- [6] A. D. Seagar, D. C. Barber, and B. H. Brown, “Theoretical limits to sensitivity and resolution in impedance imaging,” *Clinical Physics and Physiological Measurement*, vol. 8, no. 4A, p. 13, 1987.
- [7] R. Zengin, *Electrical Impedance Tomography Using Lorentz Fields*. PhD thesis, Middle East Technical University, 2012.
- [8] M. S. Gözü, “2D simulation studies and initial experimental results for hall effect imaging ,” Master’s thesis, METU, 2014.
- [9] M. Karadaş, “2D Simulations Based on the General Time Dependent Reciprocal Relation and Initial Experiments for LFEIT,” Master’s thesis, METU, 2014.
- [10] A. Montalibet, J. Jossinet, A. Matias, and D. Cathignol, “Electric current generated by ultrasonically induced lorentz force in biological media.,” *Med Biol Eng Comput.*, vol. 39, no. 1, pp. 15–20, 2001.
- [11] S. Haider, A. Hrbek, and Y. Xu, “Magneto-acousto-electrical tomography: a potential method for imaging current density and electrical impedance,” *Physiological Measurement*, vol. 29, no. 6, p. S41, 2008.
- [12] H. Ammari, Y. Capdeboscq, H. Kang, and A. Kozhemyak, “Mathematical models and reconstruction methods in magneto-acoustic imaging,” *European Journal of Applied Mathematics*, vol. 20, pp. 303–317, 006 2009.

- [13] P. Grasland-Mongrain, J.-M. Mari, J.-Y. Chapelon, and C. Lafon, “Lorentz force electrical impedance tomography,” *{IRBM}*, vol. 34, no. 4–5, pp. 357 – 360, 2013. Numéro spécial - {RITS} 2013.
- [14] L. Guo, G. Liu, and H. Xia, “Magneto-acousto-electrical tomography with magnetic induction for conductivity reconstruction,” *IEEE Transactions on Biomedical Engineering*, vol. 62, pp. 2114–2124, Sept 2015.
- [15] R. Zengin and N. G. Gençer, “Lorentz force electrical impedance tomography using magnetic field measurements,” *Physics in Medicine and Biology*, vol. 61, no. 16, p. 5887, 2016.
- [16] M. K. Pidcock, M. Kuzuoglu, and K. Leblebicioglu, “Analytic and semi-analytic solutions in electrical impedance tomography. i. two-dimensional problems,” *Physiological Measurement*, vol. 16, no. 2, p. 77, 1995.
- [17] M. K. Pidcock, M. Kuzuoglu, and K. Leblebicioglu, “Analytic and semi-analytic solutions in electrical impedance tomography. ii. three-dimensional problems,” *Physiological Measurement*, vol. 16, no. 2, p. 91, 1995.
- [18] C. Belward, T. Howes, and L. K. Forbes, “An analytic simplification for the reconstruction problem of electrical impedance tomography,” *International Journal of Imaging Systems and Technology*, vol. 12, no. 1, pp. 9–15, 2002.
- [19] D. K. Anderson, R. C. Tozer, and I. L. Freeston, “Analytic solution of the forward problem for induced current electrical impedance tomography systems,” *IEE Proceedings-Science, Measurement and Technology*, vol. 142, no. 6, pp. 425–432, 1995.
- [20] P. M. Morse and H. Feshbach, *Methods of Theoretical Physics, Part I*. New York McGraw-Hill, 1953.
- [21] B. Engquist and H. Zhao, “Approximate separability of green’s function for high frequency helmholtz equations,” tech. rep., DTIC Document, 2014.
- [22] B. Cox, “Acoustics for ultrasound imaging,” *Lecture Notes, University College London*, 2013.
- [23] M. Abramowitz and I. A. Stegun, *Handbook of mathematical functions with formulas, graphs, and mathematical tables*. US government printing office, 1964.
- [24] ITIS Foundation, “Tissue properties.” <https://www.itis.ethz.ch/virtual-population/tissue-properties/database/>. Accessed: 2016-11-30.
- [25] C. Gabriel, “Compilation of the dielectric properties of body tissues at rf and microwave frequencies.,” tech. rep., DTIC Document, 1996.

- [26] N. M. Sudharsan, E. Y. Ng, and S. L. Teh, "Surface temperature distribution of a breast with and without tumour," *Comput Methods Biomech Biomed Engin.*, vol. 2, no. 3, pp. 187–199, 1999.
- [27] D. F. Goss SA, Johnston RL, "Comprehensive compilation of empirical ultrasonic properties of mammalian tissues," *J Acoust Soc Am.*, vol. 64, no. 2, pp. 423–57, 1978.
- [28] Food and D. Administration, "Revised (510k) diagnostic ultrasound guidance for 1993," 1993.
- [29] Comsol, *Multiphysics Reference Guide for COMSOL 4.4*, 2013.
- [30] C. Gabriel, S. Gabriel, and E. Corthout, "The dielectric properties of biological tissues: I. literature survey," *Physics in Medicine and Biology*, vol. 41, no. 11, p. 2231, 1996.
- [31] S. Gabriel, R. W. Lau, and C. Gabriel, "The dielectric properties of biological tissues: Ii. measurements in the frequency range 10 hz to 20 ghz," *Physics in Medicine and Biology*, vol. 41, no. 11, p. 2251, 1996.
- [32] S. Gabriel, R. W. Lau, and C. Gabriel, "The dielectric properties of biological tissues: Iii. parametric models for the dielectric spectrum of tissues," *Physics in Medicine and Biology*, vol. 41, no. 11, p. 2271, 1996.
- [33] C. Multiphysics, "Focused ultrasound induced heating in tissue phantom, comsol multiphysics version 4.4," 1993.
- [34] J. Steketee, "Spectral emissivity of skin and pericardium," *Physics in Medicine and Biology*, vol. 18, no. 5, p. 686, 1973.
- [35] B. M. Werner J, "Temperature profiles with respect to inhomogeneity and geometry of the human body," *J Appl Physiol(1985)*, vol. 65, no. 3, pp. 1110–8, 1988.

Conference Publications

1. Ghalichi E., Zengin R. and Gençer N. G., "Heat Analysis in Magneto-Acousto Electrical Impedance Tomography," 18th International Conference on Biomedical Applications of Electrical Impedance Tomography (to be published), 2017.
2. Ghalichi E. and Gençer N. G., "An Analytical Solution for Forward Problem of Magneto-Acousto-Electrical Tomography," BioEM 2016 Conference (presented, to be published), 2016.

GRANTS AND AWARDS

2014: Research Grant and Scholarship: "Electrical Impedance Imaging Using Lorentz Fields and Magnetic Field Measurements," 114E184, Cost Action BM1309 (EMF-MED), The Scientific and Technological Research Council of Turkey (TÜBİTAK).